LEVEL ⫯ᵧ

(12)

AD A089170

DEBRIS DISTRIBUTION AS A PARAMETER IN BLAST/FIRE INTERACTION

Final Report

June 1980

Prepared by: John R. Rempel

The report has been reviewed in the Federal Emergency Management Agency and approved for publication. Approval does not signify that the contents necessarily reflect the views and policies of the Federal Emergency Management Agency.

Prepared for:

FEDERAL EMERGENCY MANAGEMENT AGENCY
WASHINGTON, D.C. 20472

DDC FILE COPY

SRI International
333 Ravenswood Avenue
Menlo Park, California 94025
(415) 326-6200
Cable: SRI INTL MPK
TWX: 910-373-1246

SRI International

80 9 8 078

REPORT DOCUMENTATION PAGE		READ INSTRUCTIONS BEFORE COMPLETING FORM
1. REPORT NUMBER	2. GOVT ACCESSION NO. AD A089 170	3. RECIPIENT'S CATALOG NUMBER
4. TITLE (and Subtitle) DEBRIS DISTRIBUTION AS A PARAMETER IN BLAST/FIRE INTERACTION.		5. TYPE OF REPORT & PERIOD COVERED Final Report. May 1979 — Jul 1980
		6. PERFORMING ORG. REPORT NUMBER HSU-8561
7. AUTHOR(s) John R. Rempel		8. CONTRACT OR GRANT NUMBER(s) DCPA01-79-C-0269
9. PERFORMING ORGANIZATION NAME AND ADDRESS SRI International Menlo Park CA 94025		10. PROGRAM ELEMENT, PROJECT, TASK AREA & WORK UNIT NUMBERS DCPA Work Unit 2564C
11. CONTROLLING OFFICE NAME AND ADDRESS Federal Emergency Management Agency Washington, D.C. 20472		12. REPORT DATE June 80
		13. NO. OF PAGES 63
14. MONITORING AGENCY NAME & ADDRESS (if diff. from Controlling Office)		15. SECURITY CLASS. (of this report) Unclassified
		15a. DECLASSIFICATION/DOWNGRADING SCHEDULE

16. DISTRIBUTION STATEMENT (of this report)

Approved for public release; distribution unlimited.

17. DISTRIBUTION STATEMENT (of the abstract entered in Block 20, if different from report)

18. SUPPLEMENTARY NOTES

19. KEY WORDS (Continue on reverse side if necessary and identify by block number)

debris, air blast, building collapse, fire/blast interaction

20. ABSTRACT (Continue on reverse side if necessary and identify by block number)

By applying the principles of classical mechanics and approximating aerodynamic and ground interaction forces, a general three dimensional debris fragment transport code DEBRIS has been written. Certain field experiments using airblast originating in large H.E. explosions have been simulated and the simulated and experimental outcomes compared. While simulation of long distance or high speed transport by tumbling or sliding over ground surfaces is not satisfactory, short distance transport such as might be found following structural

DD FORM 1 JAN 73 **1473**

EDITION OF 1 NOV 65 IS OBSOLETE

19. KEY WORDS (Continued)

20 ABSTRACT (Continued)

collapse is sufficiently realistic that DEBRIS combined with a previously developed building response code BRACOB appears ultimately capable of describing outside wall debris patterns.   It is recommended that velocity dependent loss mechanisms be incorporated in DEBRIS to improve its simulation of long distance transport and that certain existing uncertainties concerning wall debris creation and transport be lessened by means of a full size or near full size field experiment.

Accession For

NTIS GRA&I

DDC TAB

Unannounced

Justification

By

Distribution/

Avail_____

Dist.   Avail and/or
        special

DD FORM 1473 (BACK)
1 JAN 73

EDITION OF 1 NOV 65 IS OBSOLETE

DEBRIS DISTRIBUTION AS A PARAMETER IN BLAST/FIRE INTERACTION

Final Report

June 1980

Prepared by: John R. Rempel

ABSTRACT

By applying the principles of classical mechanics to approximations of aerodynamic and ground interaction forces, a general three-dimensional debris fragment transport code, DEBRIS, has been written. Certain field experiments have been simulated using airblast originating in large H E explosions and the simulated and experimental outcomes have been compared. Although simulation of long-distance or high-speed transport by tumbling or sliding over ground surfaces is not satisfactory, short-distance transport, such as might be found following structural collapse, is sufficiently realistic to enable DEBRIS and a previously developed building response code, BRACOB, to be ultimately capable of describing outside wall debris patterns. It is recommended that velocity-dependent loss mechanisms be incorporated in DEBRIS to improve its simulation of long-distance transport and that certain existing uncertainties concerning wall debris creation and transport be lessened by means of a full-size or near full-size field experiment.

SUMMARY

Starting from initial conditions originating in wall breakup, the air blast drag on a wall fragment is calculated from the simple equation giving the force in terms of a dynamic pressure q, fragment area A and empirical drag coefficient C_d:

$$F = C_d \, q \, A \quad .$$

In the case of skin fraction drag, q is based on the relative air velocity parallel to the surface and F is a force parallel to that component. Pressure drag is normal to the surface and q is calculated from the total relative air velocity. In the regime important to debris transport C_d can be treated accurately as a constant. Mach numbers never exceed approximately 0.8 and remain high only for short periods; consequently the values of C_d appropriate to incompressible flow have been used.

1

The ground is modeled as (a) a binary spring compressed by vertical displacement and (b) a source of coulomb friction acting against horizontal motion. The two spring constants (high during compression, low during decompression) have been varied to provide coefficients of restitution in the range 0.0001 to 0.01; friction coefficients in the range 0.5 to 1.1 have been studied. The ground force equations are as follows.

The spring force on the i-th corner can be written in terms of the distance z_i of the corner below the ground as:

$$F_{zi} = k_g \mid z_i \mid, \text{ provided } z_i < 0, \text{ otherwise}$$

$$F_{zi} = 0$$

where the spring constant k_g has one of two values; the friction force in terms of the spring force is:

$$\vec{F} = -\frac{\vec{V}_i - \hat{k}\,(\hat{k}\cdot\vec{V}_i)}{\left|\vec{V}_i - \hat{k}\,(\hat{k}\cdot\vec{V}_i)\right|}\ \mu F_{zi}$$

where $\vec{V}_i$ is the velocity of the ith corner relative to the ground, μ is an empirical coefficient of friction and $\hat{k}$ is the unit vector normal to the ground.

Kinematics is based on two coordinate systems, one fixed to the moving fragment and a second fixed to the ground; relative orientations of these coordinate systems are expressed at any time by means of Euler angles. Dynamics of the center of mass is separate from the dynamics of rotation:

$$M \left(\frac{d^2\vec{R}_c}{dt^2}\right)_{space} = \sum_i \vec{F}_i \tag{1}$$

and

$$\left(\frac{d\vec{L}}{dt}\right)_{body} + \vec{\omega} \times \vec{L} = \sum_i \vec{r}_i \times \vec{F}_i$$

$$\vec{L} = \begin{pmatrix} I_\alpha & 0 & 0 \\ 0 & I_\beta & 0 \\ 0 & 0 & I_\alpha \end{pmatrix} \vec{\omega} \tag{2}$$

where $\vec{R}_c$ locates the center of mass in spatial coordinates, $\vec{F}_1$ is a force on the fragment at the point located with respect to the center of mass by the vector $\vec{r}_1$ and $\vec{\omega}$ is the angular velocity about the center of mass. Moment of inertia tensors considered so far have been diagonal but not necessarily otherwise symmetrical.

In integrating equation (1) a centered scheme is used:

$$R_c (t_{n+1}) = \Delta t^2 \frac{d^2 R_c(t_n)}{dt^2} + 2R_c(t_n) - R_c(t_{n-1})$$

but because of discontinuities in the Euler angles, equation (2) for orientation is solved by an uncentered integration scheme:

$$\Delta\vec{\Omega}(t_n) = \vec{\omega}(t_n)\,\Delta t + \tfrac{1}{2}\dot{\vec{\omega}}(t_n)\,\Delta t^2$$

where Δt is the time increment and $\Delta\vec{\Omega}$ is the angular displacement of the fragment during the increment.

The realism of the three-dimensional model (the FORTRAN code of which is named DEBRIS) has been tested against experimental observations at PRAIRIE FLAT and DIAL PACK. At low overpressures and for transport over short distances, the model is very good. Simulated individual concrete masonry units (CMU) blown out of a wall at PRAIRIE FLAT by a 9 psi wave appear to travel very nearly the same distance as did the actual masonry units; the simulation of a tumbling plywood/concrete cube at DIAL PACK can be accurately simulated when peak overpressure is 15 psi. By adjustment of the coefficient, the simulation of the tumbling cube at 30 psi can be made satisfactory. However, at higher pressures (e.g., 50 and 100 psi) the simulation clearly shows the need of additional loss mechanisms than coulomb friction; a viscous or velocity-dependent force has been suggested to overcome this deficiency.

Another kind of experiment has been simulated with both the transport model and the previously developed code BRACOB (Blast Response and Collapse of Buildings). At PRAIRIE FLAT a small masonry building, 10 ft. on a side, was exposed to two peak blast pressures, 9 and 30 psi, and the final disposition

3

of wall debris was recorded photographically. Simulating the blast impact, BRACOB predicts a sequence of wall displacements and failures. With initial or departure conditions chosen by means of BRACOB and by test results clearly showing breakup patterns, the transport model can predict the impact points and final locations of wall fragments. The predicted scenario at 30 psi appears relatively unambiguous, and observed wall debris patterns are consistent with predicted patterns; apparently edge support gives rise to arching or bowing of the panel, which in turn determines the direction of departure. Fragment interaction takes place just downwind of the building.

At 9 psi the observed pattern is not symmetrical, probably due to slight assymmetries in blast or construction and, moreover, the simulation is not as clear as at 30 psi because of the predicted absence of classical air-blast flows through the building. However, simulation and observation are not inconsistent. The two codes BRACOB and DEBRIS appear to promise means of relating wall debris trajectories and final patterns to events during wall collapse.

In preparation for making estimates of urban debris, the simulation system BRACOB has been greatly enhanced. It can now handle reinforced concrete wall panels attached to yielding frames as well as reinforced walls, and storage has been increased to make analysis of office buildings and hospitals possible. A test using construction drawings of a Philadelphia hospital shows the enhanced code fully operational.

TABLE OF CONTENTS

LIST OF FIGURES

TABLES

I INTRODUCTION

Among the effects of nuclear weapons upon an urban area, those produced
by fire are probably the least understood, yet fire is undoubtedly one
of the most awesome effects. Fire researchers interested in nuclear explosions
encounter many difficulties in trying to understand fire ignition growth and
spread, not the least of which are the difficulties stemming from the effects
of blast: (1) the direct effect of blast wind and pressure on fire and
(2) the indirect effects of blast through its creation of debris. (Debris
is here defined to be any solid object displaced by blast from its normal
position or function.) It is the second of these two aspects of the fire-
blast interaction that inspired this research.

Thermal irradiation of the urban complex begins at the moment of weapon
detonation. After only an inconsequential delay, the blast wave also
departs the fireball. Because its travel to the irradiated objects is much
slower than that of the radiation, at large distances from the explosion the
two effects are readily separable in time, but at small distances the
temporal separation is not as sharp. This statement is made quantitative in
Figure 1, where the contours of thermal fluence are shown as dashed lines
in coordiantes of time on the ordinate and range or overpressure on the
abscissa. Since the thermal pulse shape is the same at all ranges, the time
axis is also marked to show certain critical times during irradiation, i.e.,
the times when fluence is 20%, 50% and 80% of the total. The heavy solid
line starting at the lower left and curving to the upper right corner repre-
sents the time of blast arrivals as a function of range. Two dissimilar
regions of overpressure are highlighted with shading. At ranges correspond-
ing to peak free-field overpressures near 50 psi (345.kPa), only 20% of the
thermal fluence has arrived by the time the blast begins to create debris;
whereas at overpressures near 4 psi (27.6 kPa), blast arrival follows the
arrival of 80% of the thermal fluence. Furthermore, assuming 20 cal/cm^2 is

1

FLUENCE, Q $\frac{cal}{cm^2}$

1000 700 500 300 200   50   20

HOB = 0

TIME, t — sec/mt$^{1/3}$

100.

10.

1.0

0.5
0.4

0.3

0.2

0.1

t_a

0.8 Q   10 t_{max}

500   200   100   50   20   10

0.5 Q

0.2Q t_{max}

80. 50. 30.   16. 12.   5.0   3.0   1.0

OVERPRESSURE P_{so} — psi

1.0   2.0   5.0   10   20   30   100

RADIUS, R — kft/mt$^{1/3}$
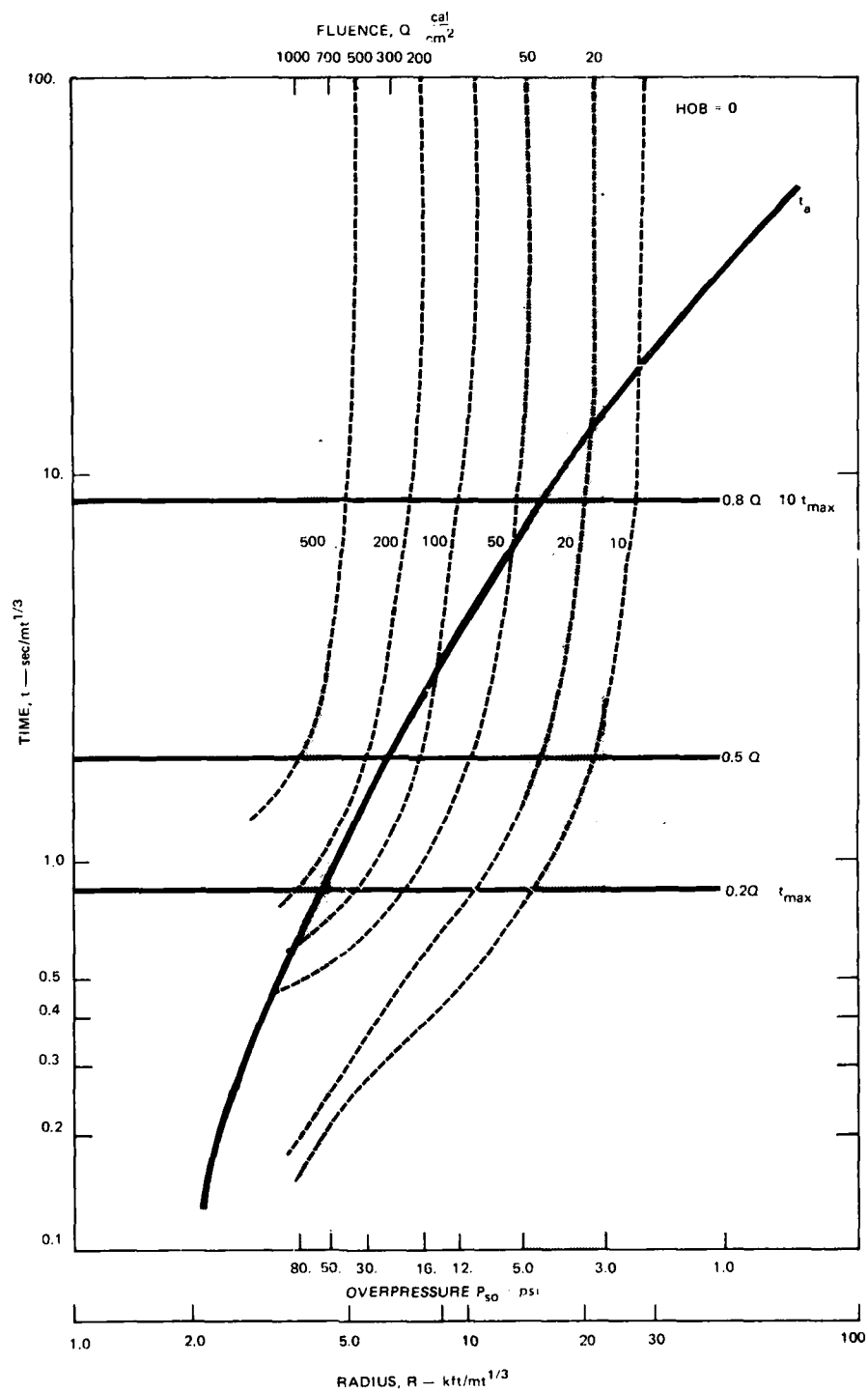
SOURCE   Effects of Nuclear Weapons, 1977

FIGURE 1   ARRIVAL TIMES OF BLAST AND THERMAL FLUENCE

2

the threshold for primary ignitions at the 4 psi-(27.6 kPa) range, such ignitions will have well over 5 s/mt$^{1/3}$ to develop before experiencing blast effects; comparable development time at 50 psi (345 kPa) on the other hand, is less by more than a factor of ten.

As time after blast arrival passes at a point in an urban complex, the problem of accurately tracing debris transport and its interaction with other debris and other structures becomes almost impossibly complicated. However, immediately after blast impact, the problem is relatively tractable and the present study begins at that point. After certain necessary theoretical and experimental preliminaries, this report addresses the problem of the conversion of the exterior walls of a building into debris and its subsequent transport.

The physical conditions determining collapse of the exterior walls of a building under airblast loading have been described elsewhere (1, 2).* The physics of transport of such debris are discussed in the next section.

---

* References are included at the end of the report.

3

II PHYSICAL PRINCIPLES OF DEBRIS TRANSPORT

Forces transporting debris fragments come from two sources: (1) blast wind
and (2) impact with the ground, walls, or other objects. The following dis-
cussion of wind forces and ground forces presents a calculation method of
predicting debris transport.

Wind Forces

Generally, the translating effects of pressure, as distinct from the wind,
are negligible on a debris fragment because the so-called "static" pressure
is short-lived against all but large objects such as building facades; debris
transport for the most part is effected by the "dynamic" pressure, q, defined as

$$q = \tfrac{1}{2} \rho u^2 \qquad (1)$$

where ρ = local air density
and u = air particle speed.

Forces on objects may be expressed in nondimensional coefficient
form in terms of lift, drag, and side-free coefficients. The force in
the windward direction is given by the drag coefficient, the dynamic
pressure, and a characteristic reference area for the body, as

$$F = C_d qA . \qquad (2)$$

In this expression F is the force in the windward direction, C_d is the drag
coefficient, and A represents the characteristic area of the body. Often A is
taken as the cross-sectional area of the object projected normal to the upstream
flow direction. The drag may be divided into components. "Pressure" drag is
created by the local fluid forces normally exerted at the surface. "Friction"
drag is created by tangential fluid friction at the surface. In magnitude, the
friction drag is generally of the order 1/10 of the pressure drag. Obviously,
the local normal pressure forces on a surface can create both drag and lift
components, depending on the orientation of the surface to the upstream wind
vector, as illustrated in Figure 2.

Let us consider a body made up of flat surfaces. The body may be divided into two parts: (1) the part that faces toward the air stream (fore body) and (2) the part that faces downstream (base region). The drag coefficient may be divided into fore body drag and what is commonly called base drag to account for the separate influences of the two parts of the body. In the present work, base drag and fore body drag have been combined. Although the pressure on a flat surface on which the flow is impinging is usually almost uniform over the surface, the pressure over a trailing flat edge may not be uniform. The resulting forces can contribute a net moment to the body while it is in flight, depending upon its orientation to the flow. The moment may result in stable or unstable flight, depending upon the location of the body's center of gravity.

Numerical values used to estimate the drag coefficient, C_d, were taken from wind tunnel data that covered a range of shapes and wind incidence angles (3, 4). The range of shapes and angles actually tested and reported in the literature is limited, but there are enough similarities between tested bodies and debris fragment shapes to make extrapolation reasonable. Also, computational simulations of reported observations of actual building debris transport serve as a rough check of the drag coefficients used.

Both friction and pressure drag coefficients depend on the dimensionless Reynolds number,

$$R_e = \frac{V_r \, \rho \, L}{\eta}$$

$$
\begin{aligned}
\text{where } V_r &= \text{relative velocity of air and object} \\
L &= \text{characteristic dimension of object} \\
\text{and } \eta &= \text{physical vicosity of air.}
\end{aligned}
$$

Figures 3A and 3B illustrate this dependence of drag on Reynolds number.
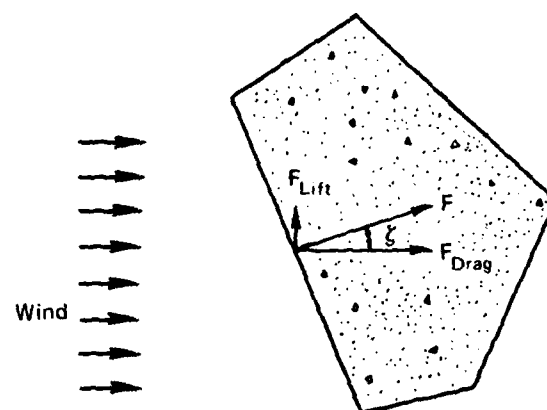
Figure 2   Drag and Lift Components of Pressure Drag Force.

Circular and Square Plates in
Normal Flow
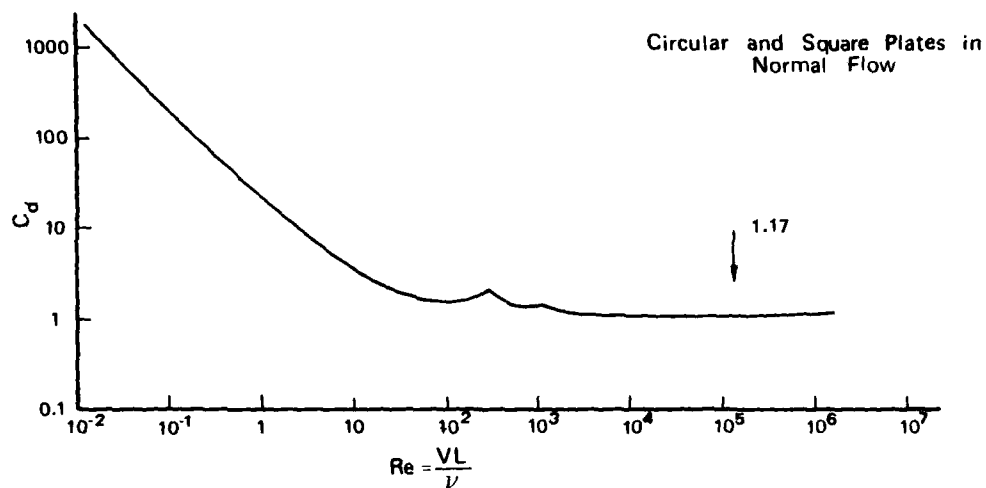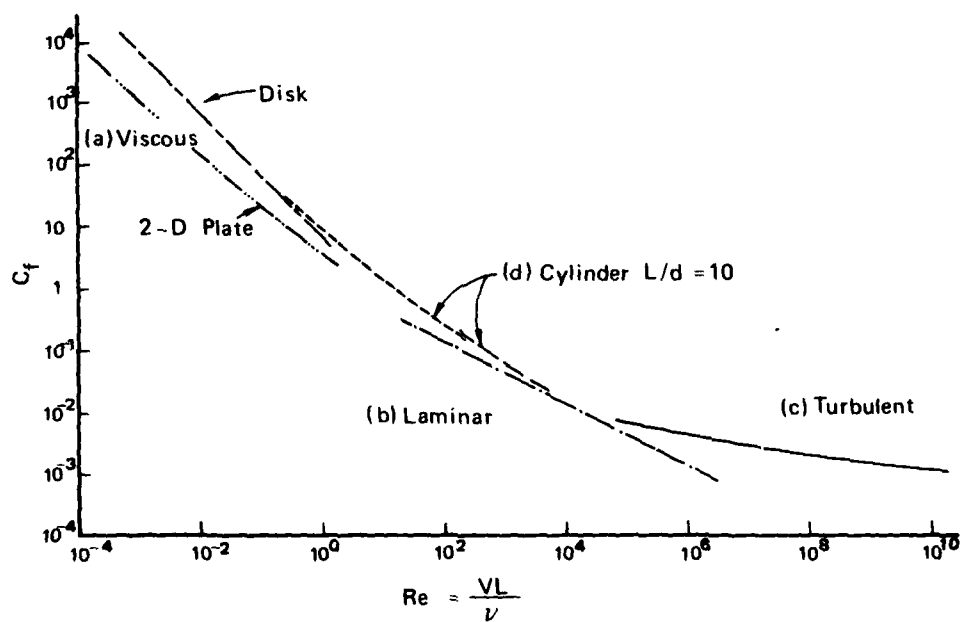
A. Pressure Drag

B. Friction Drag
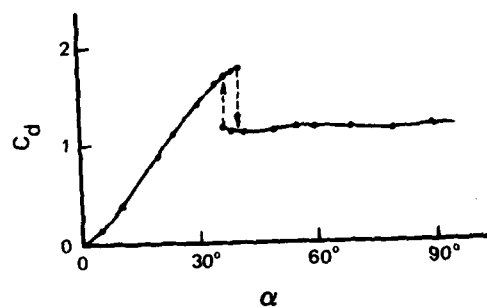
Source: Reference 3

Figure 3   Dependence of Drag Coefficients on Reynolds Number.

7

The pressure drag in (A) of Figure 3 is for a flat two-dimensional or square plate normal to the flow. The pressure drag curve is typical in that it shows high drag at low Reynolds numbers, but becomes constant at high numbers. The Reynolds numbers for the flows considered in this report are generally in the range 10^4 to 10^6. Therefore, the pressure drag coefficients will be nearly constant with Reynolds number.

Drag coefficients have been measured in wind tunnels for a number of regular shapes such as cubes, spheres, plates and cylinders. For example, such pressure drag information exists for a flat plate as a function of flow incidence angle as shown in Fig. 4. Cubes placed on a wind tunnel floor have a drag coefficient of 1.05 with one face normal to the flow and 0.90 when tilted at 45°. The lower value for a cube is approximately twice the coefficient for a sphere (0.47) (3).

Drag coefficients have also been deduced for some of these same shapes during drop tests in the atmosphere from the time of fall, with the assumption the coefficient was constant during the fall (5). For example, cubes dropped with one face down yielded values of C_d in the range 1.07 to 1.3. Terminal Reynolds numbers for these measurements were in the range 2×10^4 to 8×10^4. The study was extended to include "irregular" plates of random shape (i.e., fractures glass plates); statistically, C_d was found to differ from that for "regular" plates by no more than 5.6%, which was within the scatter of data.

Using various three-dimensional shapes made from lightweight wood, Bell Telephone Laboratories measured average drag coefficients by means of what were essentially drop tests in a vertical wind tunnel (6). The largest dimension of the objects varied from 8 to 24 inches (203 to to 610 mm), and the least wind velocity needed to hold the object in suspension was recorded. Although measured drag coefficients varied widely, they were all of the order of magnitude of unity. For example, a balsa wood cube, 8 inches (203 mm) on edge, showed an average drag coefficient of 1.5, as did a simulated cinder block made of the same material.

Source : Reference 3

Figure 4   Pressure Drag of Plate as a Function of
Angle of Impact.

9

The drag coefficients used in the present study were taken from wind-tunnel test data for "comparable" shapes, because good agreement existed between the results of drop tests and wind tunnel measurements of drag coefficients. For example, masonry units were treated as cubes; large wall fragments were considered to be flat plates. The drag coefficients of a tumbling cube were approximated to be the average between the value with the leading face normal to the flow (1.05) and the value with two leading faces 45% to the flow (0.80). The value of reference area A used in equation (2) is the maximum cross-sectional area of the body in a plane normal to the relative wind velocity. The drag coefficients for flat plates are given in Figure 4. They were corrected for Reynolds number using the values from (a) of Figure 3. Friction drag was included for all leading surfaces using the values from (B) of Figure 3. The air viscosity was computed based upon the air temperature at the fragment surface.

Ground Forces

In an attempt to model torques arising from ground impact, all calculated ground forces were considered applied to corners of the debris fragment. When by symmetry torques arising from different corners should cancel, special numerical techniques were employed to ensure they did so. Energy dissipation was provided by representing the ground as a single composite spring, relatively stiff in compression and weak in decompression (7). Values chosen for spring constants corresponded to a coefficient of restitution equal to .01. Spring compression began at the moment the corner impacted the ground, after which the spring applied increasingly upward-directed force on the corner until its downward motion reversed. At that time, the spring constant was reduced by a factor of 10^{-4}.

A second ground interaction is through sliding friction, here modeled as coulomb friction, proportional in magnitude to the force in the ground spring and a friction coefficient μ. Its direction is opposite to the

component of fragment velocity parallel to the ground surface, i.e.,

$$F = \frac{\vec{V}_{rx} + \vec{V}_{ry}}{\left| \vec{V}_{rx} + \vec{V}_{ry} \right|} \mu F_z = - \frac{\dot{x} \hat{i} + \dot{y} \hat{j}}{\left(\dot{x}^2 + \dot{y}^2 \right)^{1/2}} \mu F_z \quad .$$

This expression is written in a coordinate system in which the Z-axis is normal to the ground surface. Values of μ examined in this work varied from 0.50 to 1.1.

III EQUATIONS OF MOTION

Because debris transport is not simple downwind translation, three-
dimensional equations of motion have been written to take into account
initial displacement and rotation, ejection into crosswinds, and ground
impact forces and torques. Not yet accounted for are: fragment breakup
in flight or on impact, interactions between fragments, non-ideal airflows
such as those undoubtedly existing at least transiently around a collapsing
building, and eccentric wind forces on flat plates.

Coordinate Systems

Throughout the following discussion, reference is made to two coordinate
systems: the first fixed in space, with the Z-axis normal to the ground
surface and the Y-axis normal to the wall in its undisturbed position or
to one face of the fragment, and the second fixed to the fragment or object
transported in which unit vectors are $\hat{\alpha}$, $\hat{\beta}$, and $\hat{\gamma}$.

Before the fragment is disturbed, $\hat{\gamma}$ coincides with the unit vector $\hat{k}$ along
the Z-axis, $\hat{\alpha}$ with the unit vector $\hat{i}$ along the X-axis, and $\hat{\beta}$ with $\hat{j}$, the
unit vector along the Y-axis. Solution of the equations of motion will
then provide: (1) the instantaneous relative orientation of the two
coordinate systems and (2) the position of the center of fragment mass as
a function of time.

Any angular displacement of a rigid body can be expressed as a sequence
of the displacements through the Eurler angles $\emptyset$, θ, and ψ, illustrated in
Figure 5. (8). Once the Euler angles are known, any vector fixed in the
fragment can be expressed in the spatial coordinate system by a simple
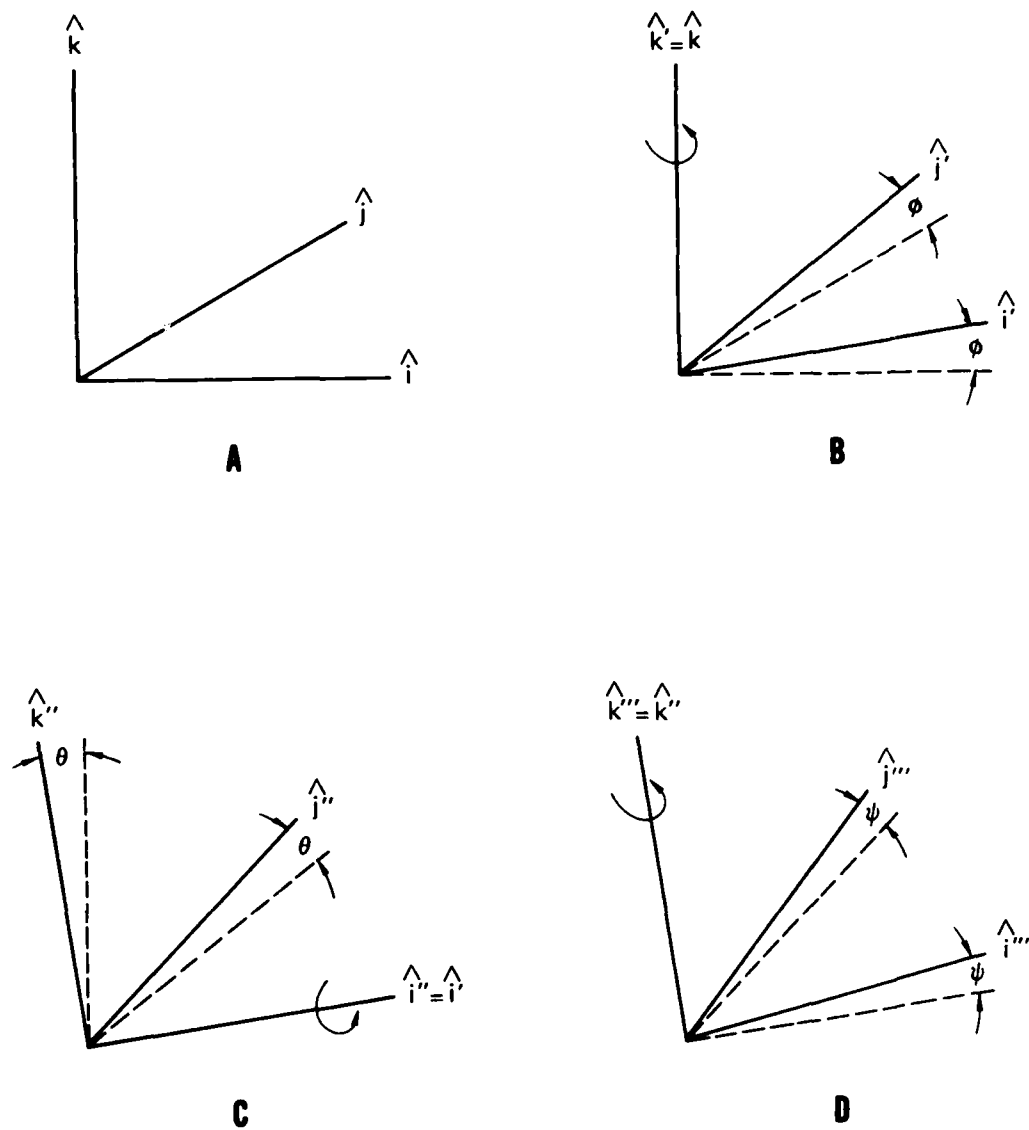tensor transformation:

12

Figure 5   Bodily Orientation Expressed by Euler Angles,
                ϕ, θ, ψ each a Function of Time.

13

$$T = M_\gamma \, M_\Theta \, M_\phi$$

where
$$M_\phi = \begin{pmatrix} \cos\phi & \sin\phi & 0 \\ -\sin\phi & \cos\phi & 0 \\ 0 & 0 & 1 \end{pmatrix} \tag{3a}$$

$$M_\Theta = \begin{pmatrix} 1 & 0 & 0 \\ 0 & \cos\Theta & \sin\Theta \\ 0 & -\sin\Theta & \cos\Theta \end{pmatrix} \tag{3b}$$

$$M_\psi = \begin{pmatrix} \cos\psi & \sin\psi & 0 \\ -\sin\psi & \cos\psi & 0 \\ 0 & 0 & 1 \end{pmatrix} \tag{3c}$$

Tensor T contains the components of the unit vectors explicity:

$$T = \begin{pmatrix} i_\alpha & j_\alpha & k_\alpha \\ i_\beta & j_\beta & k_\beta \\ i_\gamma & j_\gamma & k_\gamma \end{pmatrix} = \begin{pmatrix} \alpha_i & \alpha_j & \alpha_k \\ \beta_i & \beta_j & \beta_k \\ \gamma_i & \gamma_j & \gamma_k \end{pmatrix}$$

Dynamics

The physics of the calculation is contained in the following equations.

Motion of the center of mass follows from:

$$\vec{F} = M \left(\frac{d^2\vec{R}}{dt^2} \right)_{space} \tag{4}$$

where $\vec{R}$ is the position of the center of mass in the spatial coordinates,

M = mass of body

$\vec{F} = \Sigma \, \vec{F}_i$ the sum of all forces on the body

t = time.

The subscript "space" means $\vec{R}$ is expressed in the spatial frame.

The following equations give angular displacement as a function of time:

$$\vec{N} = \left(\frac{d\vec{L}}{dt}\right)_{space} = \left(\frac{d\vec{L}}{dt}\right)_{body} + \vec{\omega} \times \vec{L} \quad (5)$$

where $\vec{L}$ = angular momentum about center of mass (CM)

$\vec{\omega}$ = angular velocity about CM

$\vec{N} = \Sigma \vec{N}_i$, sum of all torques about CM .

Angular momentum of a rigid body is the tensor product of angular velocity and a moment of inertia tensor I:

$$\vec{L} = I \vec{\omega} .$$

Moment of inertia is a property of the distribution of mass in the body, (see reference (8) for details of calculation) but for all cases considered so far, I is diagonal, i.e.,

$$I = \begin{bmatrix} I_\alpha & 0 & 0 \\ 0 & I_\beta & 0 \\ 0 & 0 & I_\gamma \end{bmatrix}$$

in which the values of the components are here treated as constants. The derivative of angular momentum becomes:

$$\left(\frac{d\vec{L}}{dt}\right)_{body} = \hat{\alpha} I_\alpha \dot{\omega}_\alpha + \hat{\beta} I_\beta \dot{\omega}_\beta + \hat{\gamma} I_\gamma \dot{\omega}_\gamma \quad (6)$$

and

$$\vec{\omega} \times \vec{L} = \vec{\omega} \times I\vec{\omega} = \hat{\alpha} \omega_\beta \omega_\gamma (I_\gamma - I_\beta) + \hat{\beta} \omega_\alpha \omega_\gamma (I_\alpha - I_\gamma) \quad (7)$$
$$+ \hat{\gamma} \omega_\alpha \omega_\beta (I_\beta - I_\gamma)$$

where $\dot{\omega}_\alpha$, $\dot{\omega}_\beta$, and $\dot{\omega}_\gamma$ are time derivatives of the components of angular velocity in the body coordinate system. Addition of the term $\vec{\omega} \times \vec{L}$ accounts for the change of unit vectors $\hat{\alpha}$, $\hat{\beta}$, and $\hat{\gamma}$ with time.

The torque $\vec{N}$ can be written:

$$\vec{N} = \overset{i}{\Sigma} \vec{r}_i \times \vec{F}_i = \overset{i}{\Sigma} \{ \hat{\alpha}(r_{i\beta}F_{i\gamma} - r_{i\gamma}F_{i\beta}) + \hat{\beta}(r_{i\gamma}F_{i\alpha} - r_{i\alpha}F_{i\gamma})$$
$$+ \hat{\gamma}(r_{i\alpha}F_{i\beta} - r_{i\beta}F_{i\alpha}) \} \tag{8}$$

where $\vec{r}_i$ is the vector from the CM to the point of application of the i-th external force $\vec{F}_i$, and the summation is over all external forces. Dropping the subscript i, any force on the fragment can be expressed in body coordinates through the relations:

$$F_\alpha = F_x \alpha_x + F_y \alpha_y + F_z \alpha_z$$
$$F_\beta = F_x \beta_x + F_y \beta_y + F_z \beta_z$$
$$F_\gamma = F_x \gamma_x + F_y \beta_y + F_z \beta_z .$$

Integration

Since the external forces are readily calculable in terms of the spatial coordinate system, the equations of motion of the CM are integrated directly from the approximation to the second derivative, e.g.:

$$\frac{d^2 R_x}{dt^2} = \frac{1}{\Delta t} \left[\frac{R_x(t_{n+1}) - R_x(t_n)}{\Delta t} - \frac{R_x(t_n) - R_x(t_n-1)}{\Delta t} \right]$$

or

$$R_x(t_{n+1}) = (\Delta t)^2 \frac{d^2 R_x}{dt^2} + 2R_x(t_n) - R_x(t_{n-1}) . \tag{9}$$

In these expressions R_x is the x-component of the location vector $\vec{R}$ of the CM in the spatial coordinates; the argument t_n identifies the value of the displacement at the time of the n-th time step; and Δt is the magnitude of the time step, which is constant. Equation (9) provides a value of one component of CM displacement in terms of previously calculated values. There are analogous equations for the other two components.

The value of the second time derivative in equation (4) follows from equation (3).

$$\frac{d^2 R_x}{dt^2} \approx \frac{1}{M} \overset{i}{\Sigma} F_{xi} \, .$$

The unit vectors in the spatial coordinate system are constant in time.

Calculation of the fragment orientation consists of two steps:
(1) Determination of the infinitesimal rotation

$$\Delta \vec{\Omega} = \vec{\omega} \, \Delta t + \frac{1}{2} \dot{\vec{\omega}} \, (\Delta t)^2 \tag{10}$$

and (2) computation of the Euler angles expressing the new orientation at t_{n+1}. Equations of motion can be written directly in terms of first and second derivatives of the Euler angles, but the angles and their first derivatives are, in general, strongly discontinuous, requiring repeated changes of coordinate systems during numerical integration. Therefore, although the scheme represented by equation (10) employs uncentered time steps, it is far less cumbersome than an analogue of equation (9). During actual numerical integration, the accuracy of equation (10) was tested by examining the results for conservation of angular momentum.

The derivatives in equation (10) are found from equations (5), (6), and (7) after the instantaneous value of the torque $\vec{N}$ is calculated in equation (8), i.e.,

$$\dot{\omega}_\alpha = \left[N_\alpha - \omega_\beta \omega_\gamma \, (I_\gamma - I_\beta) \right] \Big/ I_\alpha$$

$$\dot{\omega}_\beta = \left[N_\beta - \omega_\gamma \omega_\alpha \, (I_\alpha - I_\gamma) \right] \Big/ I_\beta$$

$$\dot{\omega}_\gamma = \left[N_\gamma - \omega_\alpha \omega_\beta \, (I_\beta - I_\alpha) \right] \Big/ I_\gamma$$

and

$$\omega_\alpha(t_{n+1}) = \omega_\alpha(t_n) + \Delta t \, \dot{\omega}_\alpha(t_n)$$

$$\omega_\beta(t_{n+1}) = \omega_\beta(t_n) + \Delta t \, \dot{\omega}_\beta(t_n)$$

$$\omega_\gamma(t_{n+1}) = \omega_\gamma(t_n) + \Delta t \, \dot{\omega}_\gamma(t_n) \, .$$

The displacement $\Delta \vec{\Omega}$ is an infinitesimal rotation through the angle $|\Delta \Omega|$ about an axis through the CM parallel to $\Delta \vec{\Omega}$. Such a displacement can be expressed by Euler angles ϕ', θ', and ψ' in the following way (see Figure 6). The first angle ϕ' is a rotation of the body coordinate system about $\hat{\gamma}$ to align $\hat{\beta}$ with the projection of $\Delta \vec{\Omega}$ in the $\alpha\beta$ plane. The second angle θ (see Figure 5) is a rotation of coordinates about the displaced axis $\hat{\alpha}$ aligning $\hat{\gamma}$ with $\Delta \vec{\Omega}$, and finally Ψ', the Euler rotation of the body about the displaced axis $\hat{\alpha}$, is chosen so that

$$\psi' = |\vec{\nabla\Omega}|.$$

The coordinate axes $\hat{\alpha}$, $\hat{\beta}$, and $\hat{\gamma}$ are returned to their original positions in space by inverse rotations, first, $-\theta'$ about the displaced $\hat{\alpha}$ and, second, $-\phi'$ about displaced $\hat{\gamma}$. The transformation is expressed in terms of tensors similar to those defined in equation (3):

$$T^1 = M^{-1}_{\phi'} \, M^{-1}_{\theta'} \, M_{\psi'} \, M_{\theta'} M_{\phi'}$$

where

$$\phi' = \tan^{-1}\left(\frac{\Delta\Omega_\beta}{\Delta\Omega_\alpha}\right) - \frac{\pi}{2}$$

$$\theta' = \tan^{-1} \frac{(\Delta\Omega^2_\alpha + \Delta\Omega^2_\beta)^{\frac{1}{2}}}{\Delta\Omega_\gamma}$$

$$\psi' = |\Delta \vec{\Omega}|$$

when

$$\Delta\Omega_\alpha = \Delta\Omega_\beta = 0, \text{ then } \phi' = \theta' = 0.$$

The final step is the discovery of the Euler angles $\tilde{\phi}$, $\tilde{\Theta}$, and $\tilde{\psi}$ describing the new orientation as a displacement from the undisturbed position, and this is done through the tensor equation:

$$M_{\tilde{\phi}} M_{\tilde{\Theta}} M_{\tilde{\psi}} = T' M_\psi M_\Theta M_\phi = (t_{ij}) \tag{11}$$

where ϕ, Θ and ψ are the Euler angles at the preceding time step. Since t_{ij} is known, equation (11) leads to a series of equations that can be solved in the following order:
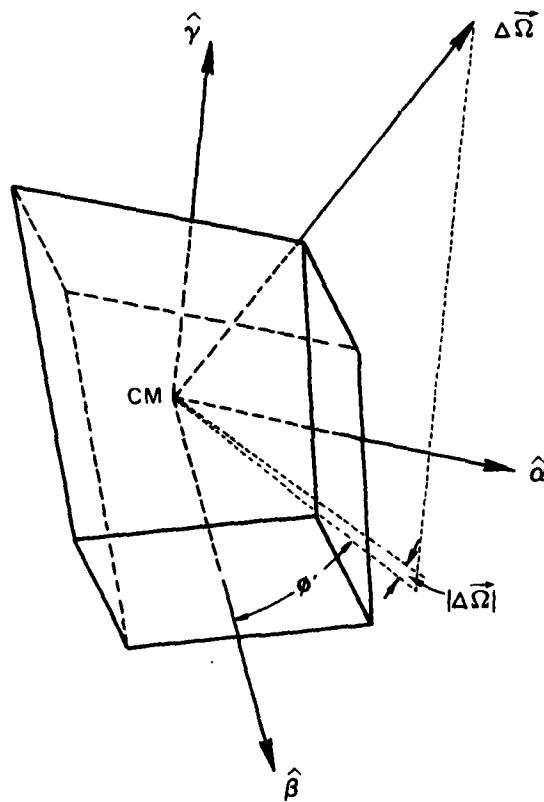
Figure 6   Infinitesimal Angular Displacement $\Delta\vec{\Omega}$.

$$\cos \tilde{\Theta} = t_{33}$$
$$\cos \tilde{\phi} = -t_{32}/\sin \tilde{\Theta}$$
$$\sin \tilde{\phi} = -t_{31}/\sin \tilde{\Theta}$$
$$\cos \tilde{\psi} = t_{23}/\sin \tilde{\Theta}$$
$$\sin \tilde{\psi} = t_{13}/\sin \tilde{\Theta}$$

when $\sin \tilde{\Theta} = 0$ then

$$\cos (\tilde{\phi} + \tilde{\psi}) = \frac{t_{11} + t_{22}}{2} .$$

The values $\tilde{\phi}$, $\tilde{\Theta}$, and $\tilde{\psi}$ become ϕ, Θ and ψ for the next integration step.

The foregoing calculational scheme has been embodied in the FORTRAN code DEBRIS
Incidentally, the values of $\tilde{\phi}$, $\tilde{\Theta}$, and $\tilde{\psi}$ calculated as above could be used to identify discontinuities in the Euler angles in the centered integration scheme outlined below.

The method is applied to the second time derivatives of the Euler angles, $\ddot{\phi}$, $\ddot{\theta}$, and $\ddot{\psi}$, which arise from the derivative of the angular velocity $\vec{\omega}$, as follows. The infinitesimal displacement $\vec{\omega} \Delta t$ may be represented by the vector sum of the three Euler rotations:

$$\vec{\omega} \Delta t = \hat{k} \Delta\phi + \hat{i}' \Delta\theta + \hat{k}'' \Delta\psi$$

or, as long as $\Delta\phi$, $\Delta\theta$ and $\Delta\psi$ are infinitesimals,

$$\vec{\omega} = \dot{\phi}\hat{k} + \dot{\theta}\hat{i}' + \dot{\psi}\hat{k}'' . \tag{12}$$

But in terms of the body coordinate system:

$$\hat{k} = \text{SIN } \psi \text{ SIN}\theta \ \hat{\alpha} + \text{ COS } \psi \text{ SIN } \theta \ \hat{\beta} + \text{ COS } \theta \ \hat{\gamma}$$

$$\hat{i}' = \text{COS } \psi \ \hat{\alpha} - \text{ SIN } \psi \ \hat{\beta}$$

$$\hat{k}'' = \hat{\gamma}$$

so that

$$\omega_\alpha = \dot{\phi} \text{ SIN } \psi \text{ SIN } \theta + \dot{\theta} \text{ COS } \psi$$

$$\omega_\beta = \dot{\phi} \text{ COS } \psi \text{ SIN } \theta - \dot{\theta} \text{ SIN } \psi$$

$$\omega_\gamma = \dot{\phi} \text{ COS } \theta + \dot{\psi}$$

and

$$\dot{\omega}_\alpha = \ddot{\phi} \text{ SIN } \psi \text{ SIN } \theta + \ddot{\theta} \text{ COS } \psi$$
$$+ \dot{\theta} \dot{\psi} \text{ COS } \psi \text{ SIN } \theta + \dot{\phi} \dot{\theta} \text{ SIN } \psi \text{ COS } \theta$$
$$- \dot{\theta} \dot{\psi} \text{ SIN } \psi$$

$$\dot{\omega}_\beta = \ddot{\phi} \text{ COS } \psi \text{ SIN } \theta - \ddot{\theta} \text{ SIN } \psi$$
$$- \dot{\phi} \dot{\psi} \text{ SIN } \psi \text{ SIN } \theta + \dot{\phi} \dot{\theta} \text{ COS } \psi \text{ COS } \theta$$
$$- \dot{\theta} \dot{\psi} \text{ COS } \psi$$

$$\dot{\omega}_\gamma = \ddot{\phi} \text{ COS } \theta + \ddot{\psi} - \dot{\phi} \dot{\theta} \text{ SIN } \theta .$$

The three equations resulting from substituting these expressions in equation (5) are:

$$\ddot{\phi} I_\alpha \text{ SIN}\psi \text{ SIN}\theta + \ddot{\theta} I_\alpha \text{ COS}\psi$$
$$= N_\alpha - I_\alpha \{ \dot{\phi} \dot{\theta} \text{ COS}\theta \text{ SIN}\psi - \dot{\phi} \dot{\psi} \text{ COS}\psi \text{ SIN}\theta$$
$$+ \dot{\theta} \dot{\psi} \text{ SIN}\psi \} + (I_\beta - I_\gamma) \{ \tfrac{1}{2} \dot{\phi}^2 \text{COS}\psi \text{ SIN}2\theta$$
$$- \dot{\psi} \dot{\theta} \text{ SIN}\psi + \dot{\phi} \dot{\psi} \text{ COS}\psi \text{ SIN}\theta - \dot{\phi} \dot{\theta} \text{ COS}\theta \text{ SIN}\psi \}$$

$$\ddot{\phi} \, I_\beta \, \cos\psi \, \sin\theta - \ddot{\theta} \, I_\beta \, \sin\psi$$

$$= N_\beta - I_\beta \{ -\dot{\phi} \, \dot{\psi} \, \sin\psi \, \sin\theta + \dot{\phi} \, \dot{\theta} \, \cos\theta \, \cos\psi - \dot{\theta} \, \dot{\psi} \, \cos\psi \}$$

$$+ (I_\gamma - I_\alpha) \{ \tfrac{1}{2} \, \dot{\phi}^2 \, \sin 2\theta \, \sin\psi + \dot{\phi} \, \dot{\theta} \, \cos\theta \, \cos\psi$$

$$+ \dot{\psi} \, \dot{\phi} \, \sin\psi \, \sin\theta + \dot{\psi} \, \dot{\theta} \, \cos\psi \}$$

$$\ddot{\phi} \, I_\gamma \, \cos\theta + \ddot{\psi} \, I_\gamma$$

$$= N_\gamma + I_\gamma \, \dot{\phi} \, \dot{\theta} \, \sin\theta + (I_\alpha - I_\beta) \{ \tfrac{1}{2} \, \dot{\phi}^2 \, \sin 2\psi \, \sin^2\theta$$

$$+ \dot{\phi} \, \dot{\theta} \, \cos 2\psi \, \sin\theta - \tfrac{1}{2} \dot{\theta}^2 \sin 2\psi \}.$$

These equations have solutions for ϕ, θ, and ψ, as long as $\sin\theta \neq 0$.
For that reason, coordinate systems (which coincide initially) may be
chosen such that the initial orientation of the fragment corresponds to
$\theta \neq 0$, π, 2π. However, during the subsequent calculation, discontinuities
in the Euler angles may arise, as can be understood by considering the
sudden onset of a torque about the β-axis. The Euler system as presently
constituted can account for an infinitesimal rotation about β only
by first introducing an exchange of coordinates (i.e., increase ϕ or θ
discontinuously by $\pm \frac{\pi}{2}$). In other words $\Delta\phi$, $\Delta\theta$, and $\Delta\psi$ in equation (12)
must be kept infinitesmal by redefining the Euler angles ϕ, θ, and ψ.

Test Cases

To test the realism of the simulation, a number of trajectories were
calculated. Every case was paralleled by an actual incident of full-scale
debris transport under loading by a blast stemming from an HE explosion
equivalent to 1 kt (4.2 TJ) nuclear (HOB = 0), for which at least partial
data exists.

Single Concrete Masonry Unit (CMU)

Two CMU walls (one of which is sketched in Figure 7) were exposed head-
on a 9-psi blast at operation PRAIRIE FLAT (6). Although one wall was

mortared and one was not, the debris patterns were very similar. Each was 5 1/3 ft (1.62 m) high and 12 ft (3.65 m) long. Using the mass distribution in a typical U.S. two-cell CMU weighing 27 lbs (12.3 kg)*, and assuming zero initial velocity, a unit in the top course is transported by blast wind a maximum distance of 13.9 ft (4.24 m) as shown in Fig. 7, when $\mu = 0.5$. Changing μ to 1.0 results in a trajectory ending at 18.5 ft (5.64 m). The greater travel results from the greater torque given the unit while in sliding contact with the ground. Apparently the relatively large torque has the effect of increasing the height of the bounce and hence the length of travel. As will be seen later, increasing the coefficient of friction μ increases energy dissipation until μ becomes unity, at which point total dissipation starts to decrease. Although no measurements of final debris locations are reported, the post-shot photograph in Figure 9 shows maximum downwind displacements consistent with that calculated for $\mu = 0.50$.

---

* Moment of inertia in CGS units is:

$$\begin{pmatrix} 0.95535 \times 10^6 & 0. & 0. \\ 0. & 0.21975 \times 10^7 & 0. \\ 0. & 0. & 0.23326 \times 10^7 \end{pmatrix}.$$
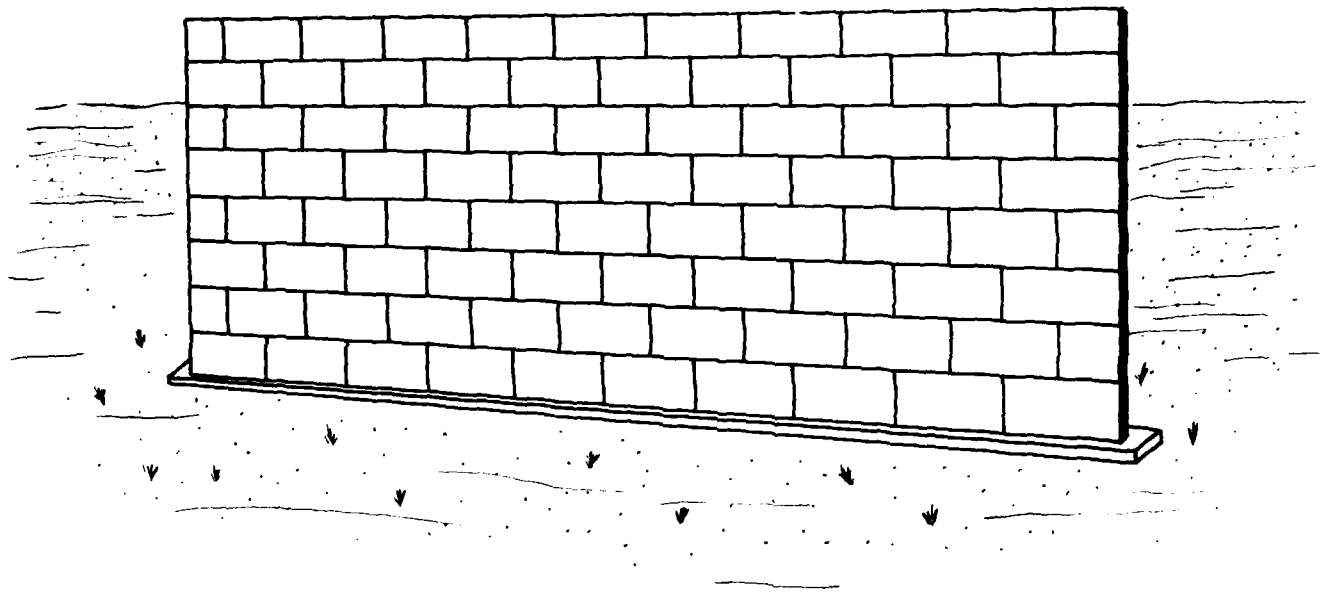
Figure 7   Preshot View   of   CMU Wall , PRAIRIE FLAT
$P_{so} = 9 \, psi$ (62 kPa).

Trajectory of center of mass
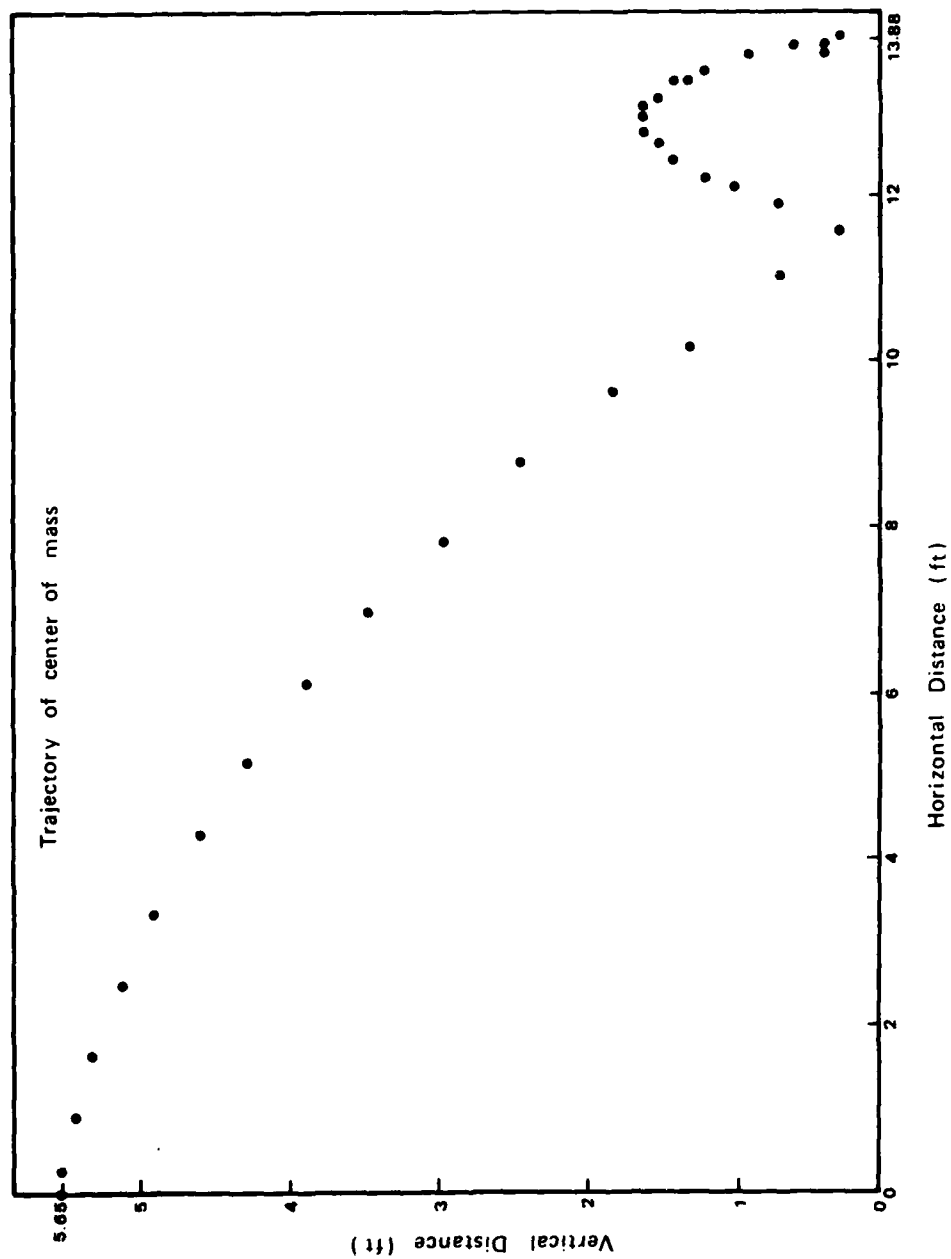
Horizontal Distance (ft)

Vertical Distance (ft)

Figure 8   Calculated Downwind Displacement of Single CMU, PRAIRIE FLAT
P_{so} = 9 psi (62 kPa).

25

Source : Reference 13

Figure 9. CMU Wall Postshot View of . PRAIRIE FLAT

P_{so} 9 psi (62 kPa).

26

In another PRAIRIE FLAT experiment, a four-walled building approximating a cube 10 ft (3.05 m) on edge (Figure 10) was exposed head-on at two overpressures, 9 and 30 psi (62.0 and 207 kPa). Although the collapse of these structures will be discussed later, the simulated flight of a single CMU from the sidewall will be used here to demonstrate conservation of angular momentum and indicate the power of debris analysis. A unit in the top course was assumed to depart the wall 54 ms after a 30-psi (207-kPa) blast impact with a velocity of magnitude 69 ft/s (21.0 m/s) directed normally to the blast wind. The calculated trajectory of the CM is represented in Figures 11A and 11B. Figure 11A presents the projection of the trajectory in the plane normal to the ground and parallel to the wind while Figure 11B gives the projection of the trajectory in the plane normal to the wind. The CMU was still moving after a crosswind travel of 85 ft (25.9 m) and travel of 24 ft (7.315 m) downwind. Wind reversal occurs before the unit strikes the ground but does not reverse the downwind CMU motion until near the end of the flight. Ground friction μ in this case was 0.90.

Conservation of angular momentum was tested after the second ground impact at 1.4301 s or 6,621 calculational cycles after the first ground impact at 0.7680. Results are tabulated in Table 1.

Table 1

CONSERVATION OF ANGULAR MOMENTUM

Time (s)	L_x (cgs)	L_y	L_x
1.4301	-0.5138×10^8	0.3710×10^7	-0.4081×10^7
1.5301	-0.5144	0.3666	-0.4106
1.6301	-0.5150	0.3692	-0.4057
1.7301	-0.5156	0.3723	-0.4113
1.8301	-0.5163	0.3670	-0.4104
1.9301	-0.5169	0.3723	-0.4076

Constancy of angular momentum is probably good enough for present purposes and a major effort to improve the integration accuracy is not justified.
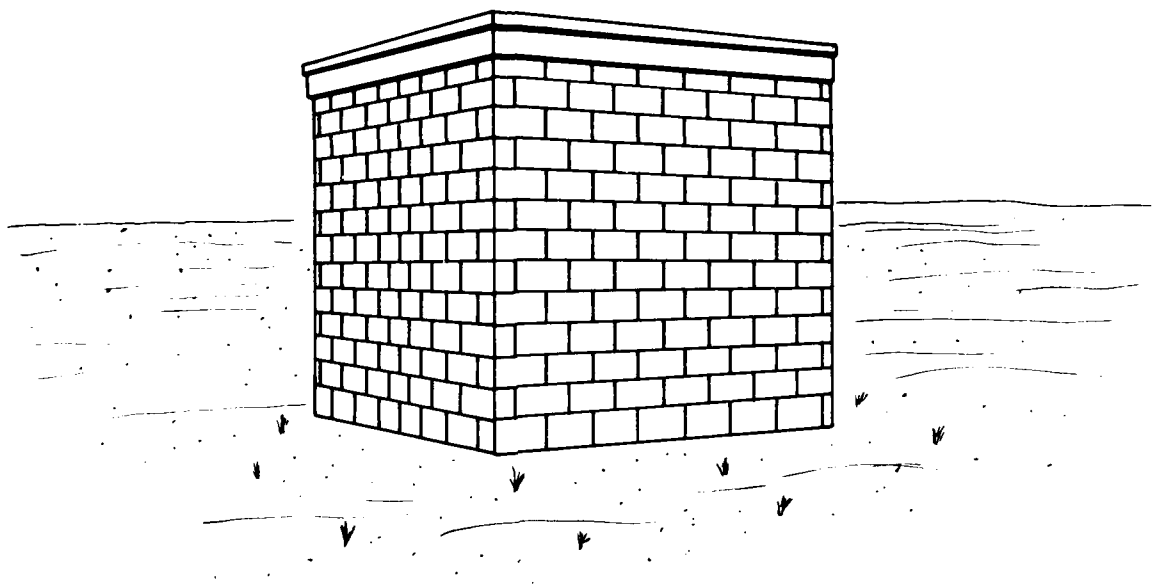
27

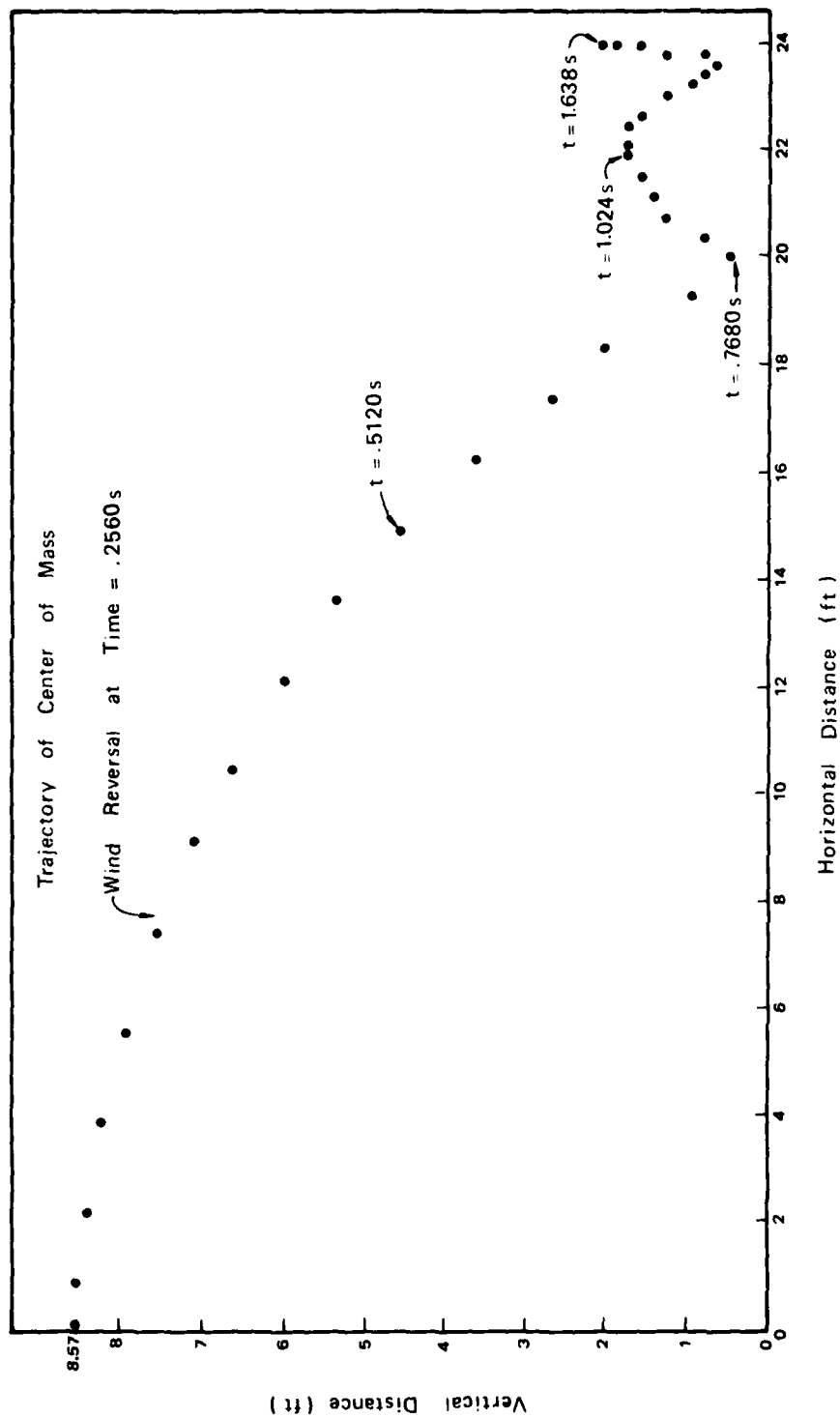Figure 10   CMU Windowless Buildings,   PRAIRIE   FLAT.

Trajectory of Center of Mass

Wind Reversal at Time = .2560 s

t = .5120 s

t = .7680 s

t = 1.024 s

t = 1.638 s

Horizontal Distance (ft)

Vertical Distance (ft)

Figure 11 A   Simulated Trajectory of Single CMU from Top of Sidewall (Downwind)
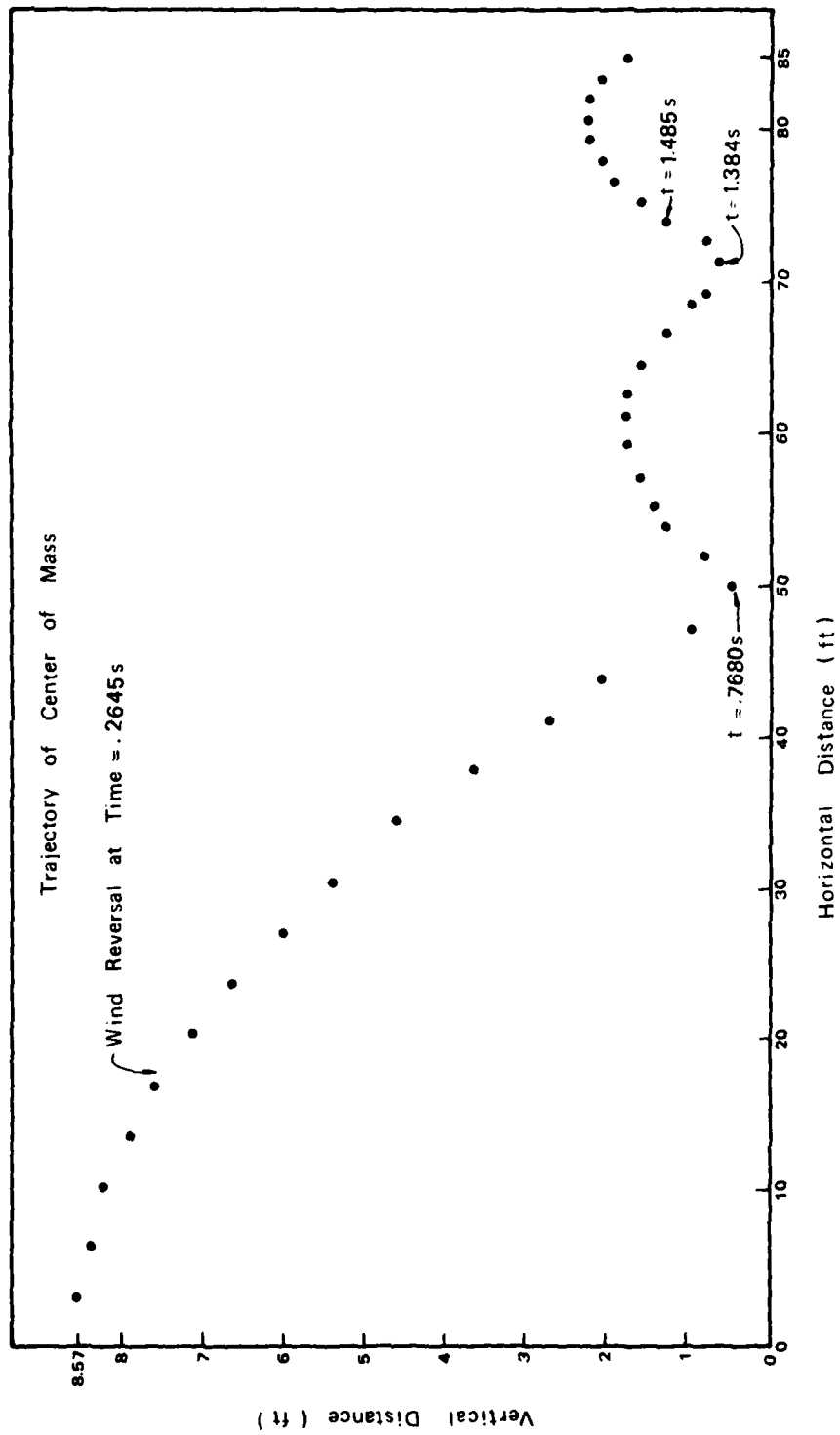$P_{so} = 30$ psi (207 kPa).

29

Figure 11B   Simulated   Trajectory of   Single   CMU   from   Top   of   Sidewall (Crosswind)
P_{so} = 30 psi (207 kPa) .

30

An interesting plot of the calculated angular displacement of the vector $\hat{Y}$ during the interval 1.78 to 1.92 s is shown in Figure 12. The projection of the vector in the x - y plane is marked by the dashed line. The lack of symmetry in the inertia tensor prevents true precession.

Starting the CMU with the same initial speed and departure time, but half-way up the sidewall instead of in the top course, and allowing it to come to rest before stopping the calculation, results in a final downwind displacement of 19 ft (5.79 m) and crosswind displacement of 93 ft (28.3 m) after 4.47 s of travel (Figures 13A and B). As the postshot photograph in (figure 14B) shows, this appears to be an unrealistically large amount of travel, suggesting either the sidewall does not break up by ejecting CMU directly into the crosswind or that the initial conditions are in error. For example, changing the initial conditions to a start at 54 ms with a speed of 34 ft/s (10.4 m/s) results in net displacements of 11.6 ft (3.53 m) downwind and 25.6 ft (7.80 m) crosswind, which are clearly more realistic. In both these examples, the unit had no initial angular momentum. Later, the effects of hinging at a support will be explored. As an example of another extreme, initial conditions on the same unit, equal to a speed of 5 ft/s (1.52 m/s) at the departure time of 54 ms yielded a final resting place at 0.847 s equal to a downwind displacement of 10.4 ft (3.17 m) and a crosswind displacement of 2.40 ft (0.732 m). From Fig. 14B, such a result does not seem to have been likely for units originally located in the center of the sidewall.

Through transport calculations of this kind and some postshot debris distribution data, it appears possible to deduce the sequence of wall failure and even something about the mode of failure.

Plywood/Concrete Cube (DIAL PACK)

At operation DIAL PACK, over a dozen plywood cubes filled with concrete were placed on the ground at the 15, 30, 50, and 100 psi (103, 207, 345 and 689 kPa) contours, and final downwind displacements recorded (9). The cubes weighed approximately 65 lbs (29.6 kg) and were 1 ft (.305 m) on edge. The ground was not smoothed but left natural. Judging from their final attitudes, the cubes travelled by tumbling motion. There are
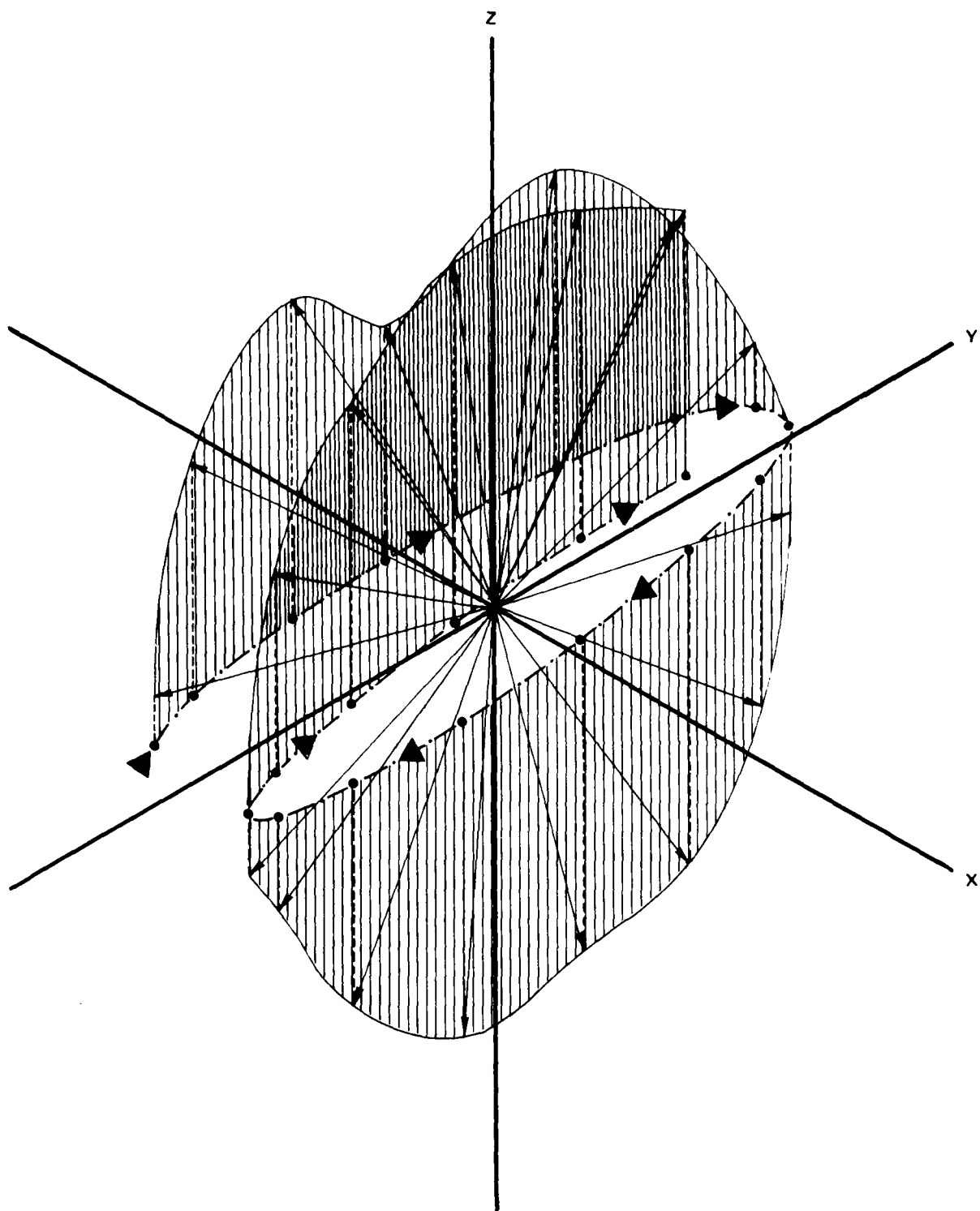
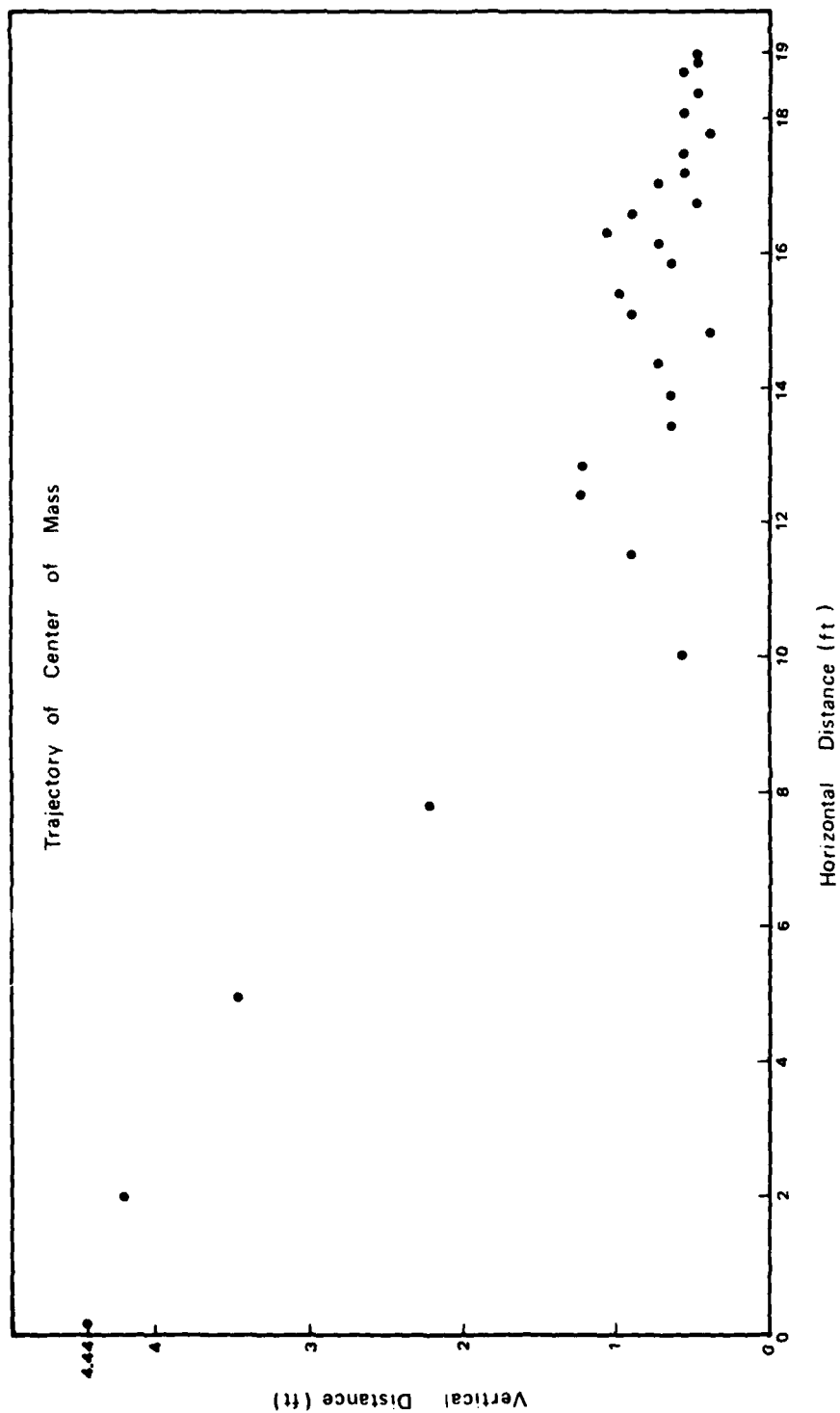Figure 12   Orientation of Concrete Masonry Unit in Free Flight.

Trajectory of Center of Mass

Horizontal Distance (ft)

Vertical Distance (ft)

Figure 13A   Simulated   Trajectory   of   CMU   from   Middle   of   Sidewall   (Downwind)

P_{so} = 30 psi (207 kPa).

33

Trajectory of Center of Mass

Vertical Distance (ft)

Horizontal Distance (ft)
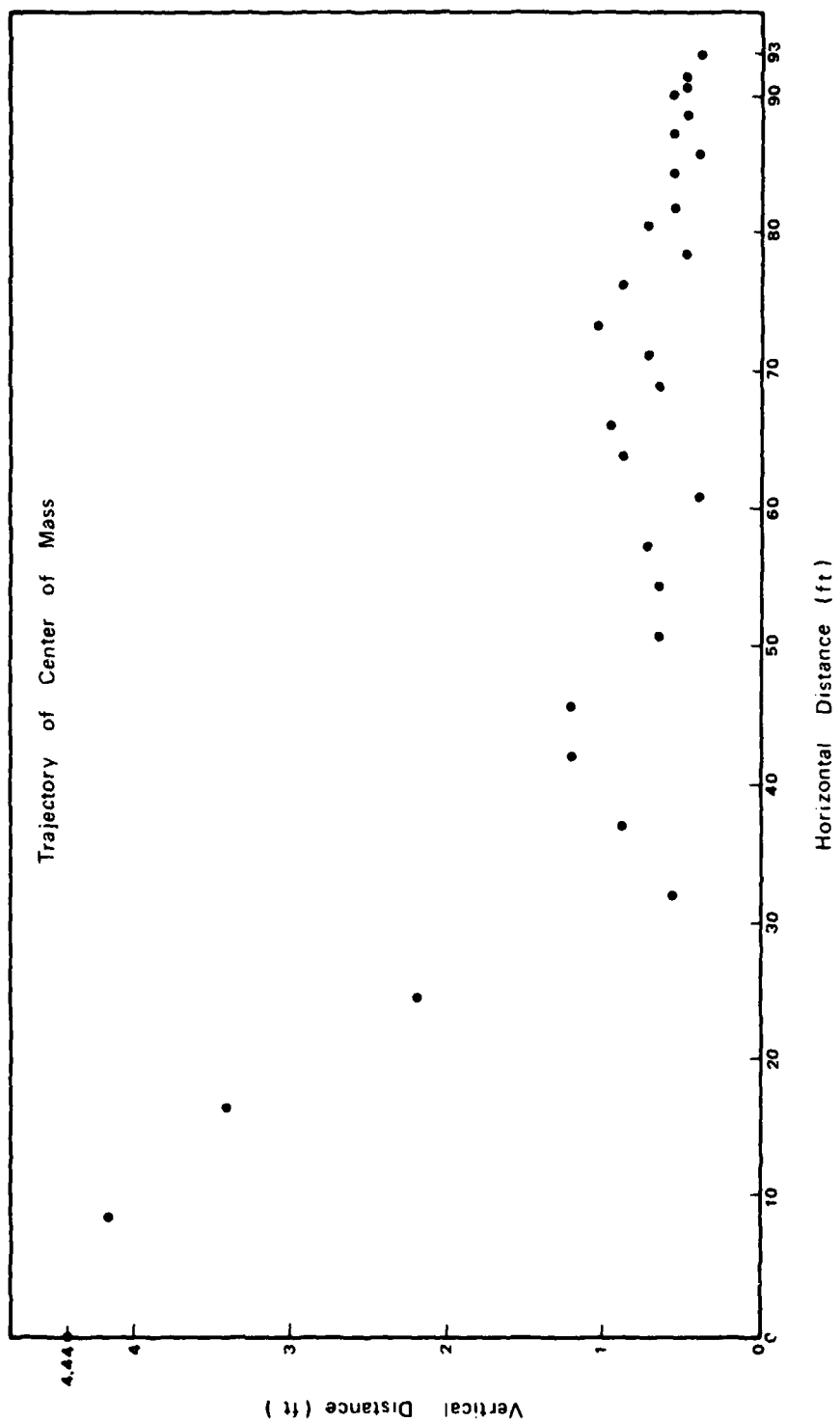
Figure 13B   Simulated Trajectory of CMU from Middle of Sidewall (Crosswind)
P_{so} = 30 psi (207 kPa).

34

Source: Reference 13

Figure 14 A   Postshot View of CMU Building , PRAIRIE FLAT

P_{so} = 9 psi (62 kPa).

Source: Reference 13

Figure 14B   Postshot View of CMU Building , PRAIRIE FLAT
P_{so} = 30 psi (207 kPa).

36

no motion pictures available, so far as is known.

Before DEBRIS could be used in the simulation of tumbling cubes, it was modified to account for attenuation of peak blast pressure with range from ground zero.

In the simulation at 15 and 30 psi (103 and 207. kPa) the cube came to rest before overturning except when the coefficient of friction μ reached or exceeded 1.0. As expected, the distance travelled declined as μ = 1.0, at which point the downwind displacement rose, as can be seen in Table 2.

Table 2

SIMULATED PLYWOOD/CONCRETE CUBE
Downwind Displacement

Coefficient of Friction μ	Displacement			
	15 psi (103. kPa)		30 psi (207 kPa)	
	(ft)	(m)	(ft)	(m)
0.50	15.3	2.10		
0.75	11.6	3.54		
0.90	10.1	3.08	41.0	12.5
0.95	4.14	1.26	39.2	11.9
1.00	>10.5	3.20	63.8	19.4

In all the cases presented in the table, airblast pressure drag when there was no tumbling was C_d = 1.05. Ground spring constants were K_{g1} = 2009 $\frac{lb}{in}$ (3.5 x 10^8 $\frac{dyne}{cm}$) and K_{g2} = .201 $\frac{lb}{in}$ (3.5 x 10^4 $\frac{dyne}{cm}$). For tumbling cubes or cube-like shapes a drag coefficient averaged over edge-on and head-on attitudes, i.e., C_d = $\frac{1.05 + 0.80}{2}$ = 0.925, was used. In every case the drag force was based on presented area and base drag was considered to be included in C_d. Within the limits of variation of K_{g1} and K_{g2} explored, the influence of the ground spring on net downwind translation of the cube appeared small. Definitive work on the effect of spring

constants remains to be done.

The trajectory plotted in Figure 15 shows clearly why the net downwind displacement becomes larger for $\mu = 1.0$ than for $\mu < 1.0$: a high value of friction coefficient can produce a simulation of tumbling. When $\mu \lesssim 0.95$ the trajectory corresponding to that of Figure 15 is flat.

Figure 16, summarizing the results of these cube observations and calculations, makes it clear that the simple coulomb friction model is inadequate in cases of long distance translation. For studying wall and building collapse, however, where transport is over relatively short distances, the present simulation is satisfactory. In Fig. 16 the solid curve is drawn through the average of the values of net downwind displacement of cubes observed in the field as a function of the incident overpressure at their original location. The observed values themselves are represented by solid dots. The simulated displacements appear as crosses ($\mu = 0.95$) and crosses in circles ($\mu = 1.0$). Differences between calculation and observation increase dramatically with incident overpressure, suggesting that a velocity-dependent or viscous loss model may be appropriate (10). In fact, Figure 16, as well as the results previous simulations, indicate that in the short range $\mu = 0.50$ is the best choice; viscous forces apparently become important only at high speeds.
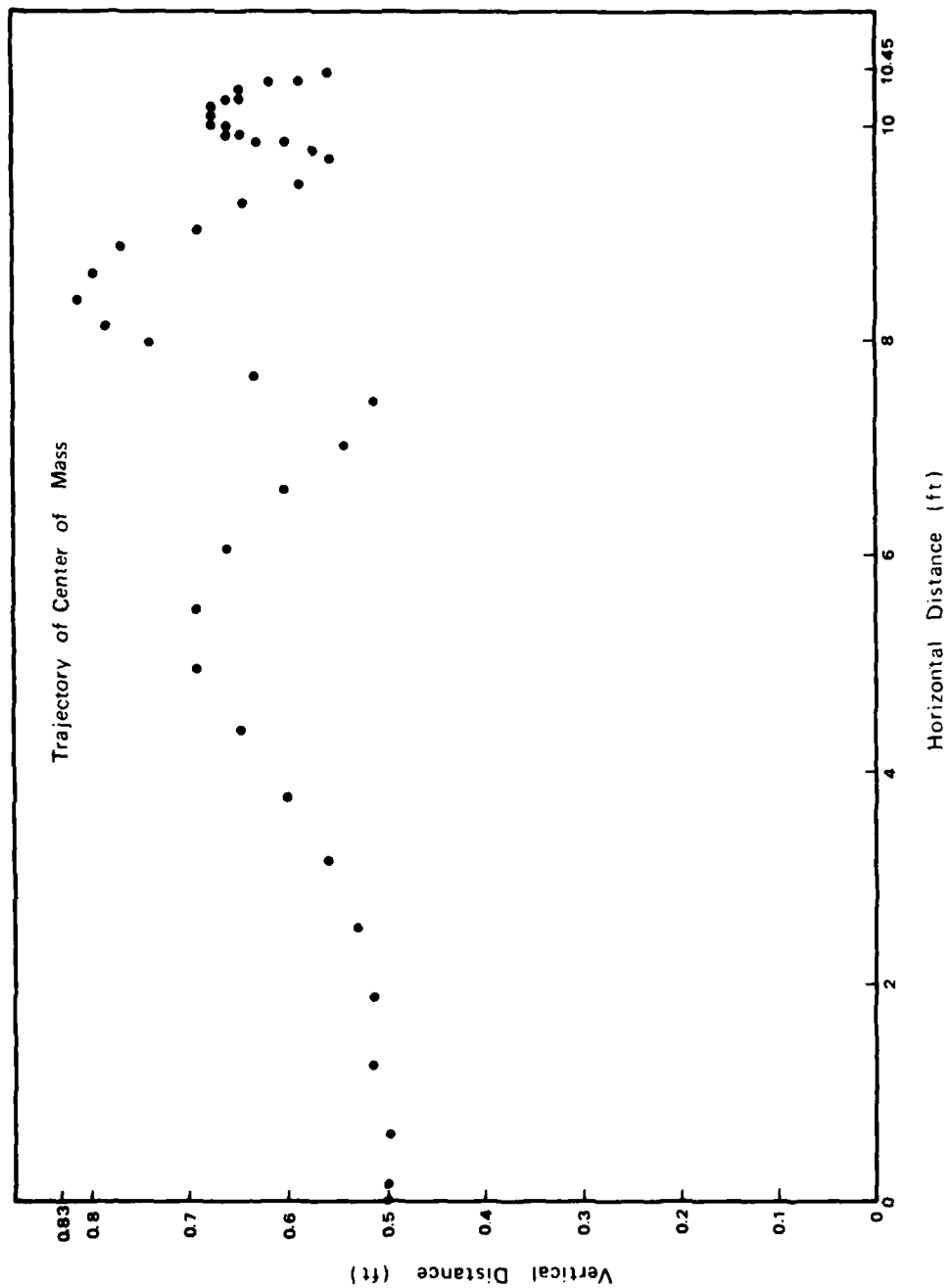
38

Figure 15   Calculated Trajectory of Tumbling Cube.   DIAL PACK
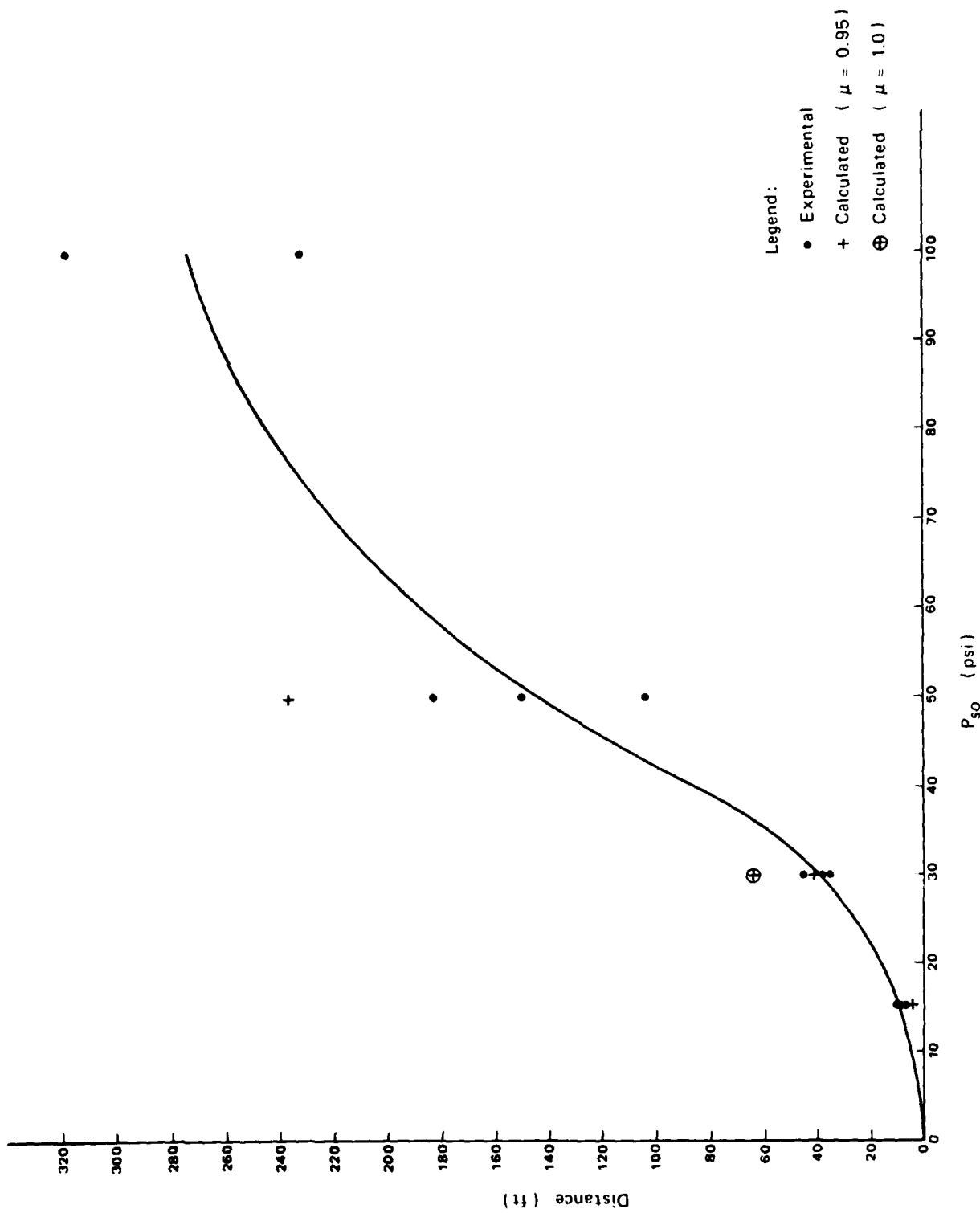P_{so} = 15 psi (103 kPa), μ = 1.0.

Figure 16   Simulated Translation of Plywood/Concrete Cube, DIAL PACK.

Legend:

• Experimental

+ Calculated ($\mu = 0.95$)

⊕ Calculated ($\mu = 1.0$)

40

IV COLLAPSING BUILDINGS

The source of debris of concern to civil defense is the partial or complete collapse of buildings after an airblast. The easiest source of wall debris to analyze with tools developed to this point is probably the masonry, load-bearing structure. The earliest observation of the collapse of a full-size, four-wall structure of this kind occurred at Operation TEAPOT (11). Partial collapse was observed at 5 psi (34.5 kPa) when the sidewalls apparently fell outward due to poor anchorage against outward motion and blast entry from the high reflected pressure against the front of the building. The front elevation was much less damaged. Downwind translation of the sidewall debris was not great, indicating relatively late failure. In any case, this early observation is not a good one for present purposes. Of more interest are the four-walled structures analyzed at Operation PRAIRIE FLAT (12). These were of two kinds. The first was an approximately cubical structure 10 ft (3.05 m) on edge made of one tier of mortared CMU carrying a light wood roof (Figure 10). Although some of these buildings had relatively large windows, this discussion deals only with the windowless examples. The second was a five-foot, cubical roofed structure made of plastic interlocking blocks glued together only at the corners of the building (Figure 17 and 18).

CMU Building, Prairie Flat

Although the incipient collapse overpressure of the CMU Building has not been calculated, it must be quite low. Exposed at two locations, i.e., 9 and 30 psi (62.0 and 207 kPa), it was easily and completely demolished by the blast at both places (13). The two postshot photographs (Figures 14A and 14B) are the only data found so far that describe the result of these experiments. Any postulated sequence of collapse events based on such a limited amount of evidence must be extremely tentative.
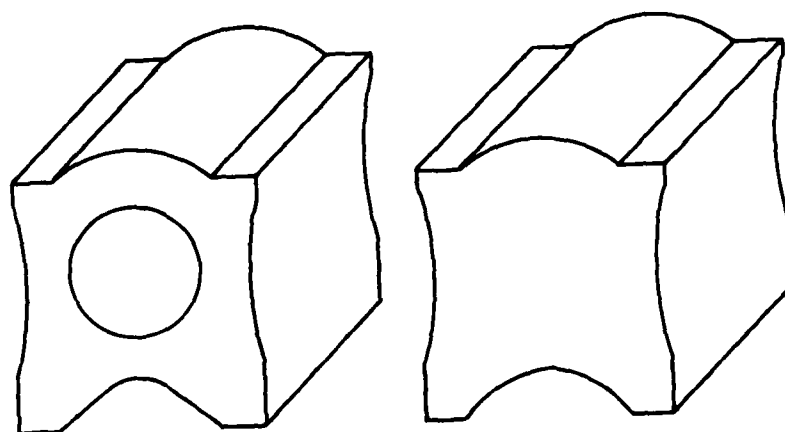
PRAIRIE FLAT (1/8 Scale)
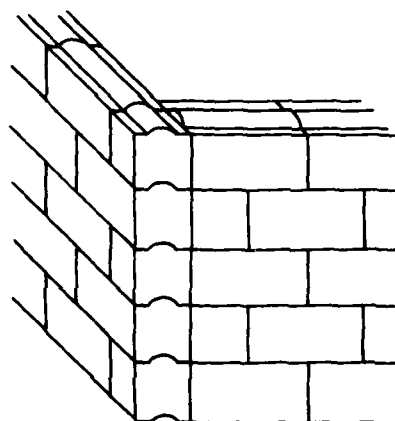
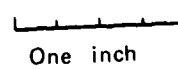Corner Sections Glued
before Blocks Laid

Glue

Source :   Reference 12

Figure 17   Plastic Block Building, PRAIRIE   FLAT.

42

PRAIRIE FLAT (1/8 Scale)

One inch

Source :   Reference 12

Figure 18   Plastic Blocks, PRAIRIE FLAT.

43

BRACOB, short for Blast Response and Collapse of Buildings, is a computer code designed to treat simultaneously blast impact, reflection and clearing, room-filling or backloading, as well as wall deflection and collapse throughout one floor of a building (14). As the simulated blast front sweeps over the building, the appropriate external and internal wall loads are applied as functions of time. Upon collapse of a wall, the interior pressures against certain of the remaining walls are adjusted to the levels prevailing outside the collapsed wall. At this stage in its development, the calculation uses an arbitrary delay between the instant of wall failure (i.e., when it can no longer support a vertical load) and the time of transfer of the exterior pressure to the interior. The magnitude of this delay can determine the final disposition of wall debris and, at present, there is no certain way of calculating it.

Figure 19 presents the result of a BRACOB simulation of the impact of the 30-psi (207-kPa) blast against the PRAIRIE FLAT CMU building. The arbitrary delay used in transferring exterior pressure to interior was 4 ms.* In the figure the solid line represents a wall before deflection and the dashed line shows schematically the deflection of the wall (either inward or outward). The deflection is deliberately shown as zero at the vertical wall edges and greatest at the center to represent the bowing or "arching" of horizontally loaded walls supported at the edges.** When the solid line disappears, the wall has "collapsed", i.e., the time delay of 4 ms after "failure" has passed.

According to Figure 19, collapse of the front

---

* Values of other structural wall parameters during this simulation were:
  - Support case 2
  - Modulus of rupture, 12.9 psi (88.9 kPa)
  - In-plane vertical lead, 10.5 lb/in (188 kg/m)
  - Modulus of elasticity, 3×10^6 psi (2.07×10^7 kPa)
  - Density, 110.6 pcf (1775 kg/m^3)
  - Thickness, 7.63 (.194m).

** Photographic data exist that illustrate the cracking, deflection, and collapse of single wall panels for test purposes. Usually, in these cases
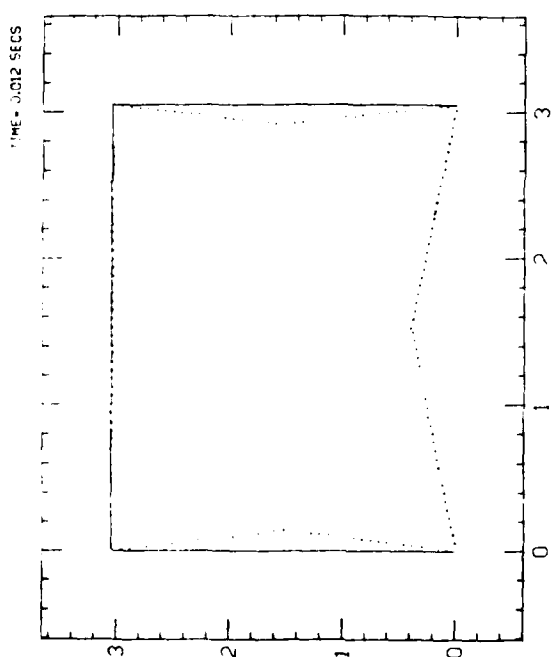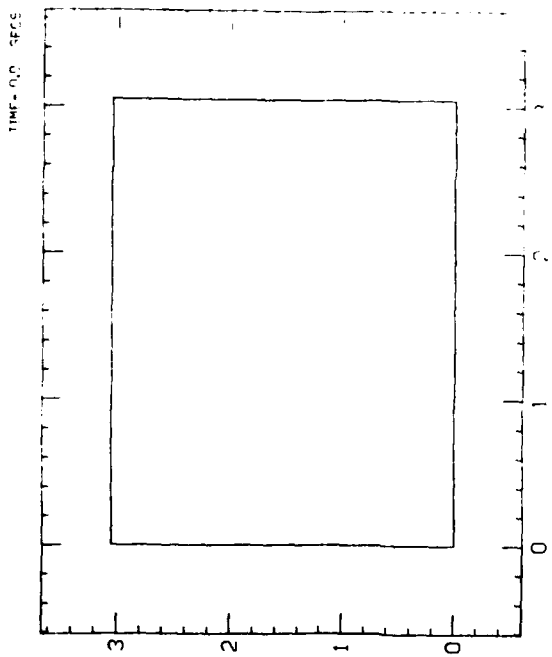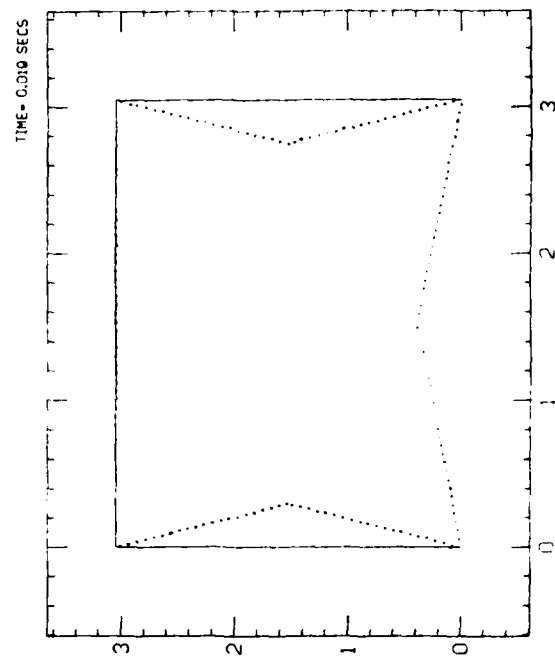
Figure 19 Simulated Collapse of CMU Building, PRAIRIE FLAT
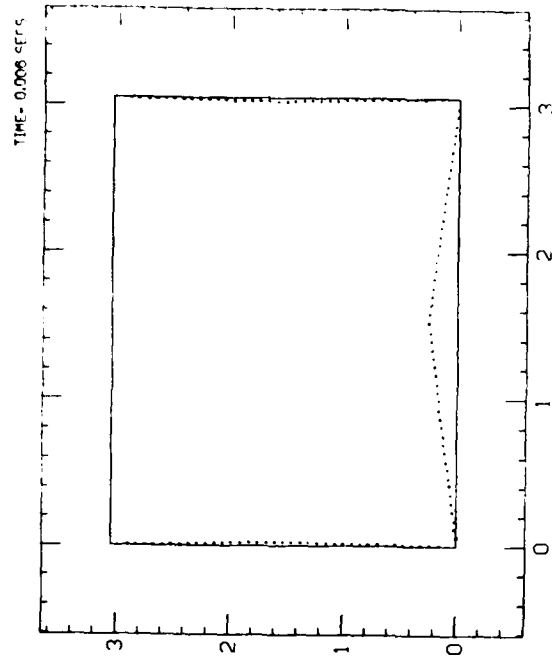$P_{so} = 30$ psi (207 kPa) (DLY = .004 s).

45

TIME= 0.031 SECS

TIME= 0.038 SECS

TIME= 0.025 SECS

TIME= 0.032 SECS

(Continued)

46

TIME = 0.050 SECS

TIME = 0.058 SECS

TIME = 0.044 SECS

TIME = 0.059 SECS

(Concluded)

47
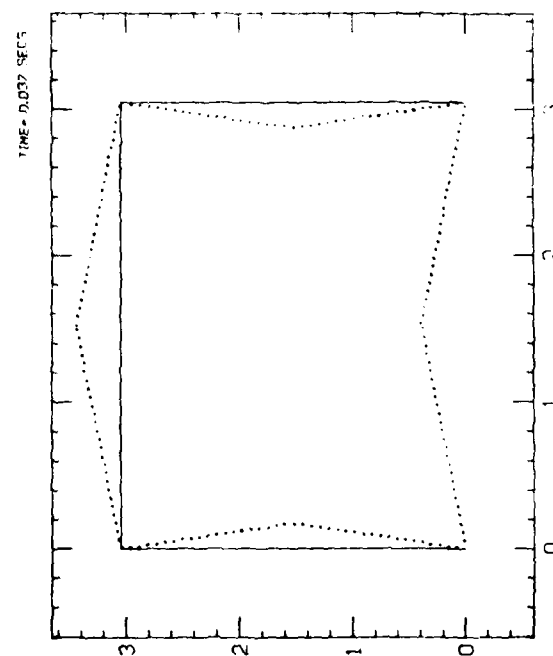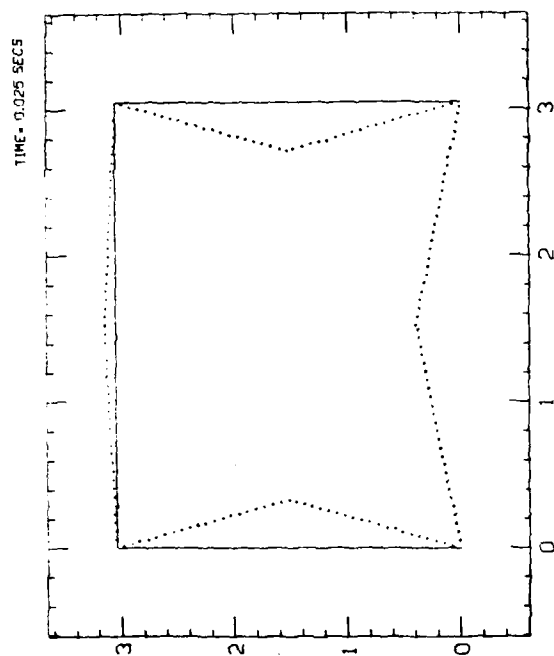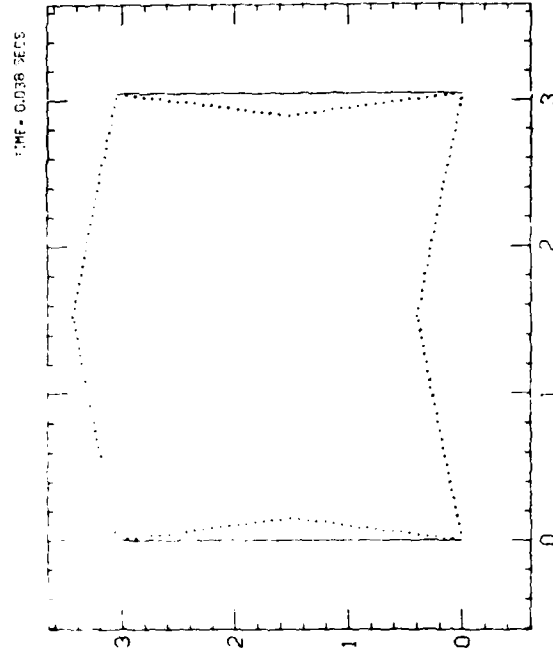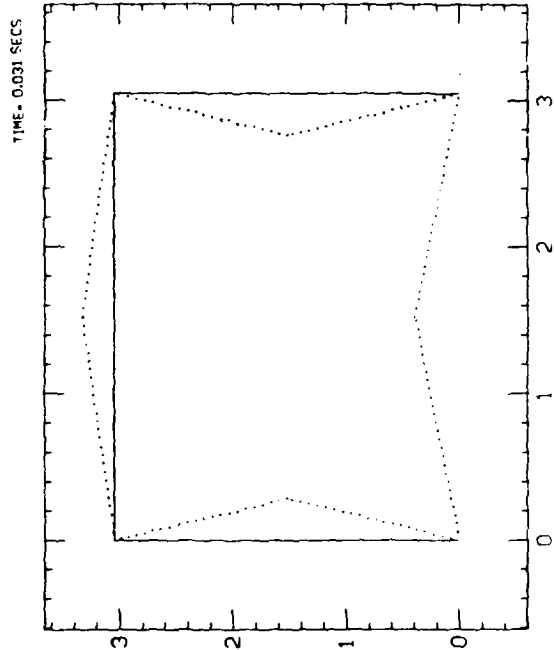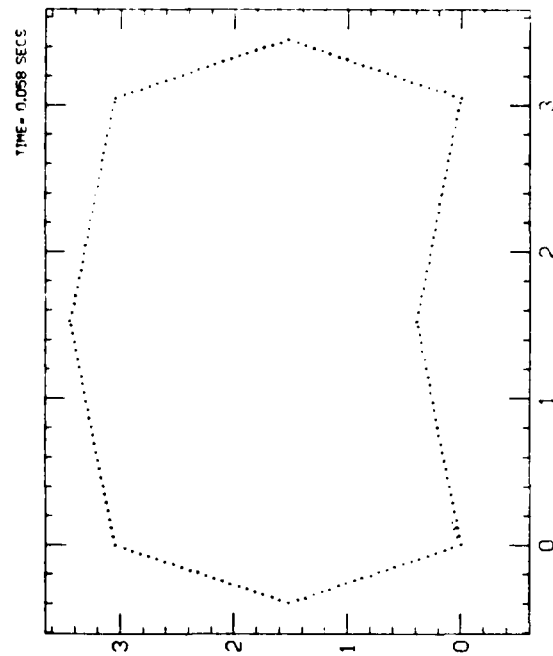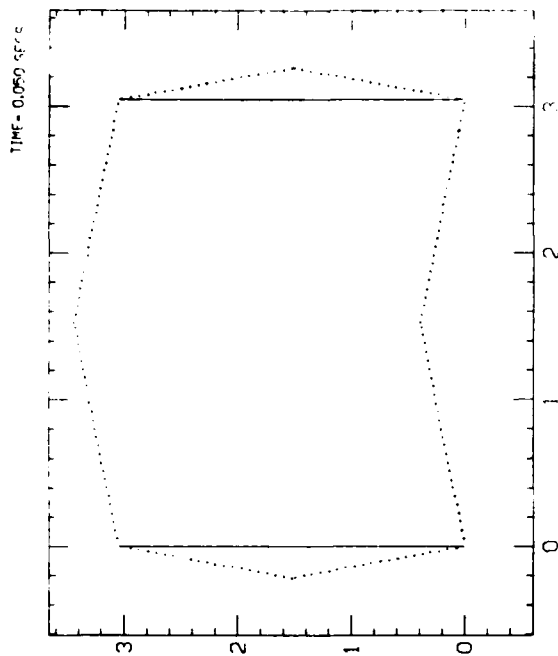
wall takes place at 12 ms after blast arrival, when the side walls are still moving inward and the rear wall is hardly disturbed. Since there are no windows, collapse of the front wall provides the first backloading of the walls, unless blast has entered through the roof. At 19 ms the sidewalls are near the point of maximum inward deflection. Under normal circumstances they would now begin to move outward, more or less reversing (except for hysteretic effects) their inward path. However, the front wall is now "collapsed" although it is too early to see the opening cleared of debris. It is very likely 11 ms after front wall "failure" there is a substantial amount of support still present at the leading edges of the sidewalls. How long this continues is not known, but the subsequent sequence of events in the sidewalls (as calculated by BRACOB and represented in Figure 19 for times greater than approximately 40 ms) does not seem to be consistent with the debris pile in Figure 14B. After 44 ms BRACOB shows the sidewalls arching outward as if fully supported at the front edges. This is probably unrealist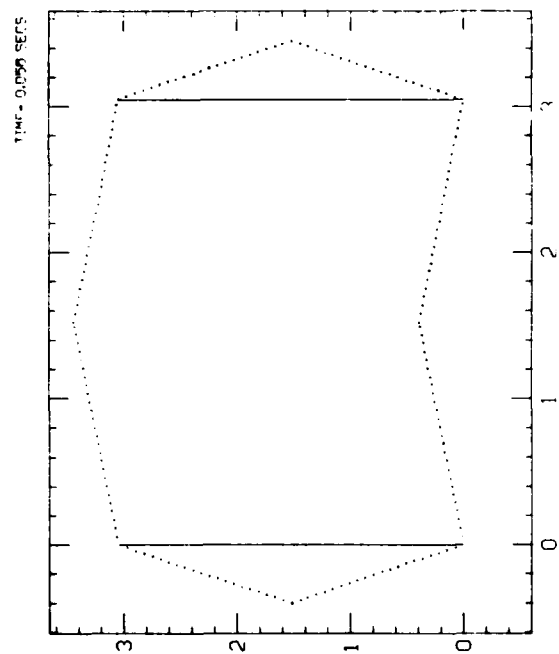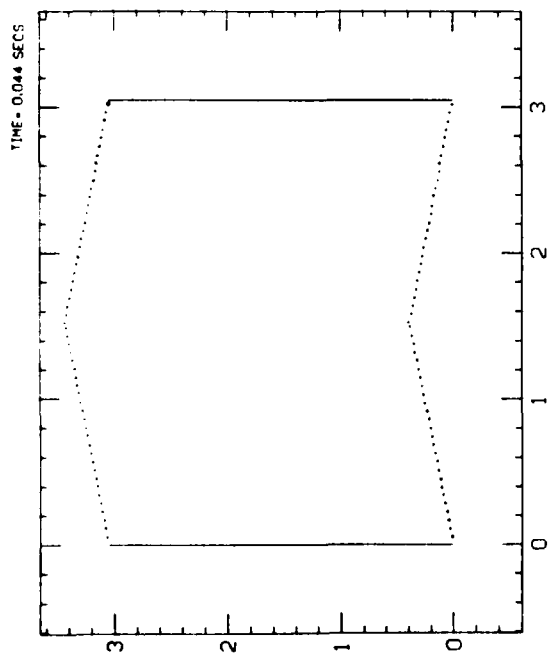ic. On the other hand, BRACOB also shows the rear wall collapsing at 39 ms. If this does in fact happen at that time, the blast wind (still early in its positive phase) will blow through the structure and catch the inwardly arched sidewalls.

Simulations with DEBRIS indicate a subsequent translation to positions of (a) first ground contact and (b) final resting place in the general

---

** the panel interacts in some way with a rigid or nearly rigid frame along its edges. One such test was performed at the 4.5-psi (31.0-kPa) contour at Shot Encore, Operation Upshot-Knothole. Some of the crack patterns in masonry panels seen in motion pictures from Encore are sketched in Figure 20 (15). Fragments are varied in shape but there are generally two classes: those that are "hinged" along an edge due to the support and those that are punched straight out. Usually, the latter kind are found near the center of the panel. (In examining these crack patterns it must be remembered that the panels tested at Encore were supported in an entirely different manner than those in the PRAIRIE FLAT CMU house: the failure patterns may be quite different. Note also that the arching drawn in Figure 19 represents a two-dimensional effect, i.e., the figure cannot show the bowing that may be occurring in a vertical plane.)

48

Panel No. 5

Left
Standing

Left
Standing
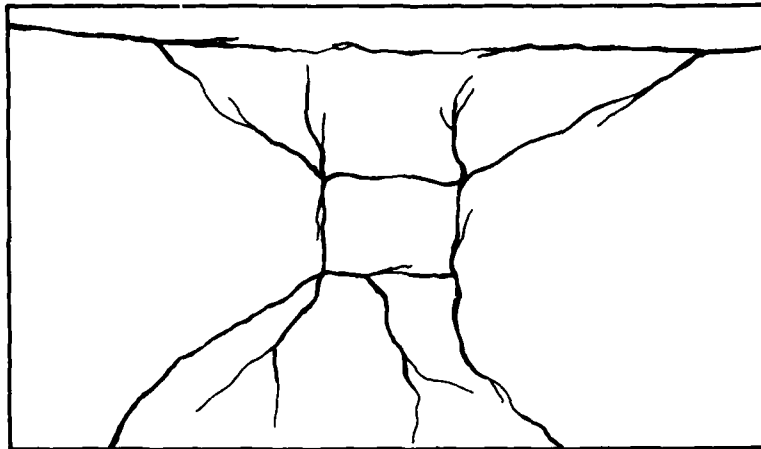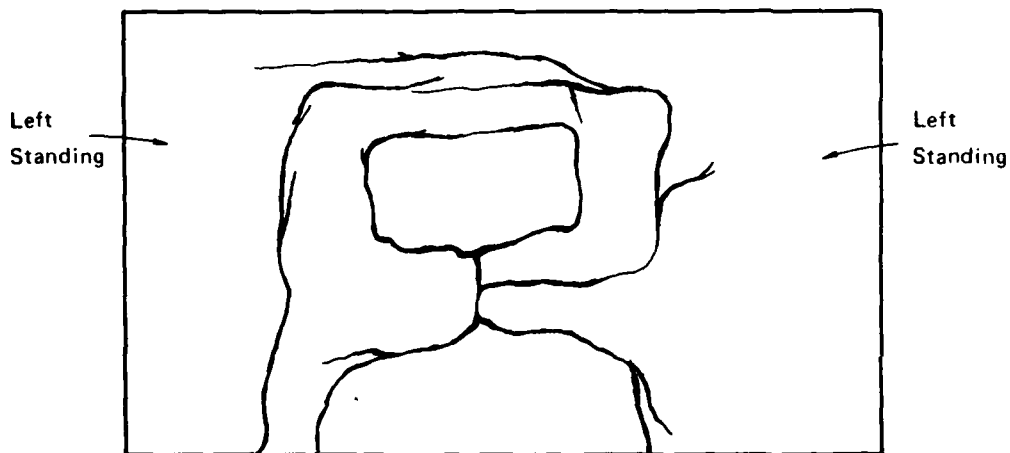
Panel No. 9

Figure 20   Wall Crack Patterns, Shot ENCORE
$P_{so} = 4.5$ psi (31 kPa).

49

area suggested by Figure 14B, i.e., outward and downstream. There is some dependence on the exact position and speed of the inwardly arching sidewall fragment at the moment it is caught by the through flowing blast and on the degree of edge support at the front wall still existing at that moment. Assuming all support is lost at time t_c and that inward speed and deflection are V_i and y_i, respectively, then displacements, ΔX and ΔY, found by DEBRIS are shown in Table 3. Displacements to first ground contact and to final resting place are reported. These results are for fragments originally receiving support at the vertical edge (side hinge) on the GZ side. ΔY and ΔX refer to crosswind and downwind travel, respectively. Z_c is the original height above ground of the CM. Predictions by DEBRIS are evidently consistent with at least part of the debris pattern in Figure 14B. There are, of course, fragments from the portion of the sidewall that hinges at the vertical edge away from GZ. It is not clear when this material is exposed to the flow-through but it is reasonable that it is translated to the rear of the building site.

These displacements are sketched in Figure 21.

Disposal of the front wall debris is also important, especially if it strikes the rear wall before the rear wall fails. BRACOB predicts front wall failure at 8 ms when inward speed at the central point is 47 ft/s (14.3 m/s). An unhinged fragment not in ground contact originally passes the position of the rear wall at 100 ms. Since this is the first kind of front wall fragment to cross the depth of the building, the interaction between fragments from front and rear walls most probably takes place well downwind of the building site. Incidentally, first ground contact of a simulated unhinged front wall fragment 2 ft x 2 ft (.610 m. x .610 m) with Z_c = 5.0 ft (1.52 m) occurs at 75 ft (22.9 m), and at 319 ft (97.2 m) downwind it is still moving. There is certainly no evidence of such enormous transport in Figure 14B., suggesting the importance of viscous ground losses, fragment-fragment interaction, or errors in the estimates of departure times or speeds.

Table 3

SIMULATED SIDEWALL FRAGMENT DISPLACEMENTS OF CENTERS OF MASS, SIDE HINGE

$(P_{so} = 30 \text{ psi})$

| | | Departure Conditions | | | Net Displacements (ft) | | | |
| | Fragment Size (ft) | Height Z_c (ft) | Speed V_i (fps) | Time t_c (ms) | First Hit or Flat on Ground Δx | Δy | Final Location Δx | Δy |
Simulation								
1	5 x 5	2.5	0.0	50	flat 3.5	5.6	4.0	6.9
2	5 x 5	2.5	0.0	38	flat 4.5	6.9	5.4	9.0
3	5 x 5	3.5	0.0	38	hit 2.0	3.0	2.8	9.5
4	3 x 3	1.5	0.0	38	flat 6.2	8.8	12.3	17.5

51
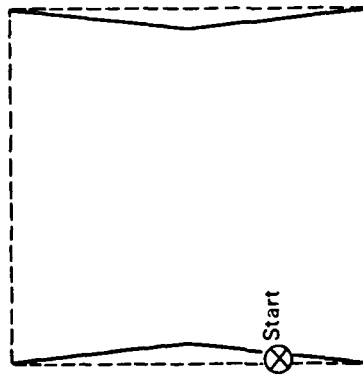
Figure 21   Simulated Sidewall Fragment Displacement of Center of Mass, Side Hinge
$P_{so} = 30\,psi$ (207 kPa).

52

Side- and bottom-hinged fragments from the front wall have also been simulated. (There appeared to be essentially no structural support at the roof, thus a top-hinged fragment was not simulated). A simulated side-hinged fragment from the front wall originally in contact with the ground is flat on the ground at a downwind displacement equal to 35.1 ft (10.7 m) and at a lateral displacement toward the hinge equal to 11.4 ft (3.47m). While still partially upright, this simulated fragment passes the position of the rear wall at 109 ms. Its lateral displacement at that time is 2.4 ft (.731 m). At that same time a simulated bottom-hinged fragment from the rear wall is less than 5.2 ft (1.58 m) downstream and a simulated side-hinged fragment near the rear wall is displaced less than 1 ft (.304 m) laterally and about 5 ft (1.52 m) downwind. The potential for debris interaction (and greater energy dissipation than calculated by BRACOB) is thus significant. However, it would appear in any case that the initial fragment speeds derived from BRACOB are excessive and lead to unrealistically large downwind transport from front and rear walls.

The data in the 9-psi (62-kPa) experiment (Figure 14A) are less clear than those taken from the 30-psi (207-kPa) experiment (Figure 14B). For one thing, the righthand sidewall in Figure 14A appears partially intact. Also, evidently, the front wall debris did not clear the building site.

A BRACOB simulation of the PRAIRIE FLAT CMU building in a 9-psi (62-kPa) blast predicts wall collapse times and directions as follows*:

Wall	Time	Direction
front	17.7 ms	inward
side	30.0	inward
rear	156.0	outward

At the time the side walls fail, the rear wall is inwardly deflected 1.5 inches (38 mm). Thus, if the simulation is at all close to reality, there does not appear any likelihood that the collapsed side walls will be caught in classical blast flowing through the building. Since positive overpressure
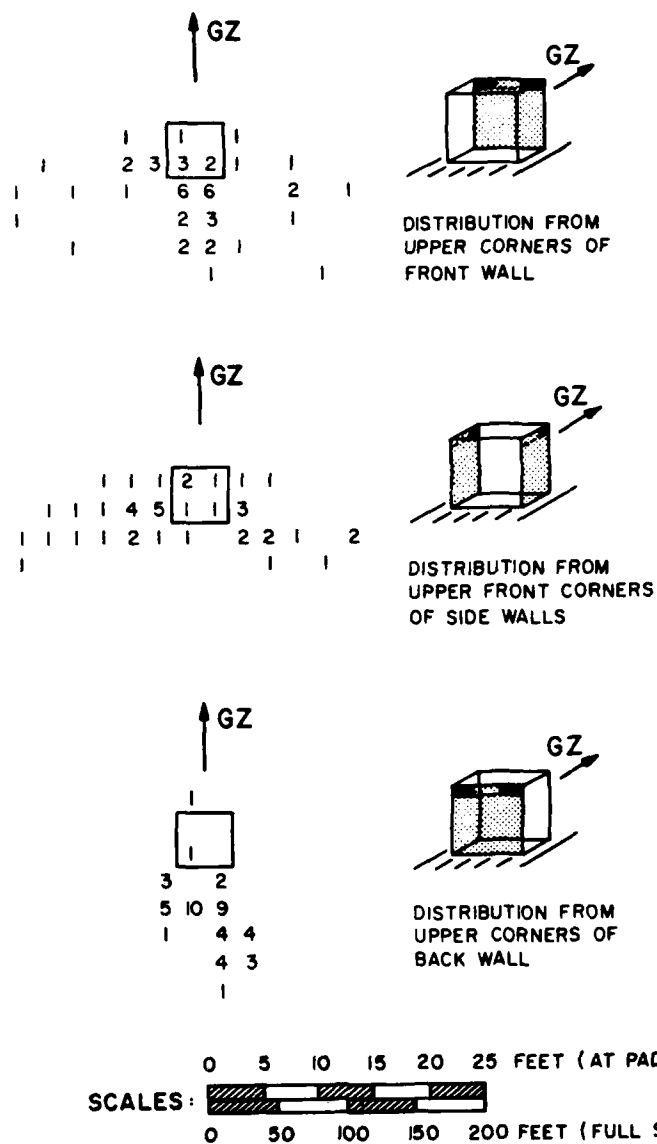
---

* Delay for debris clearance at the front wall was taken to be zero in this simulation

phase duration was approximately 250 ms, it is likely, however, that the rear wall debris went downstream of the building and such a disposition accords with Figure 14A. Although no simulations with code DEBRIS of this event have as yet been made, the long positive phase duration probably means that enough drag exists at a very late time to push some of the inwardly collapsed side wall fragments outward, and this too is consistent with the observed debris distribution on the left side of the building in Figure 14A.

Plastic Block Model Building

These models, exposed to 3 and 6 psi (20.7 and 41.4 kPA) at PRAIRIE FLAT, were designed to provide airblast debris similar to that from larger masonry buildings. No BRACOB simulations of collapse have been attempted, but a cursory examination of the debris data reported from these experiments reveals a pattern of distribution similar to that already seen in the CMU buildings. A tiny sample of this voluminous data is reproduced in Figure 22, from which it appears clear that arching in these models took place. The glued corners created realistic support conditions. The first sketch shows expected lateral displacement due to vertical edge support. The kind of rearward and lateral displacement in the second sketch seems to confirm the expectation of early blast flow-through while the sidewall is displaced inward (as postulated in Figure 19). And finally, the distribution in the third sketch suggests an outward failure of the rear wall while vertical edge support from the sidewalls still existed.

DISTRIBUTION FROM
UPPER CORNERS OF
FRONT WALL

DISTRIBUTION FROM
UPPER FRONT CORNERS
OF SIDE WALLS

DISTRIBUTION FROM
UPPER CORNERS OF
BACK WALL

SCALES:
0   5   10   15   20   25 FEET (AT PAD)
0   50   100   150   200 FEET (FULL SIZE)

Source: Reference 12

Figure 22. Observed Debris Distribution from Plastic Block Models,
PRAIRIE FLAT, P_{so} = 3 psi (20.7 kPa)

55

V ENHANCEMENT OF BRACOB

The present effort included a substantial enhancement of BRACOB in preparation for the calculation of urban debris distributions. *Storage was increased to handle large buildings and capability was added to treat reinforced concrete and masonry walls arching in a yielding frame (16).*

To test the new capabilities, a partial response to a 30 psi-(207-kPa) head-on blast was simulated for one floor of the Henry R. Landis State Hospital in Philadelphia. An elevation of the wing that was studied is shown in Figure 23. A typical floor plan was simplified and analyzed in terms of an orthogonal grid (Figure 24) and grid intervals taken from construction drawings (Table 4). Finally, Figure 25 contains two computer-drawn floor plans of the typical floor of the hospital after blast arrival. (Interior doors are treated as closed.) Collapse of the front walls at this pressure is almost immediate.
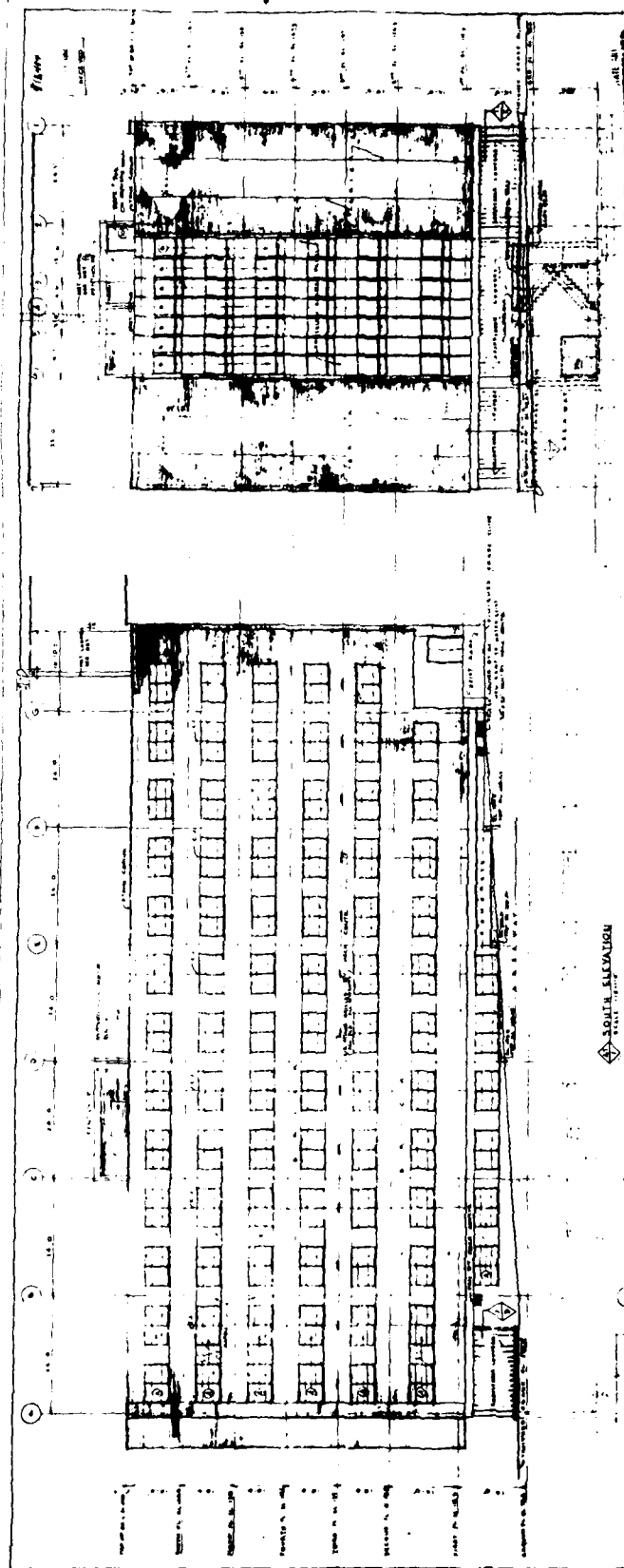
Figure 23. Henry R. Landis State Hospital, Philadelphia, Elevation
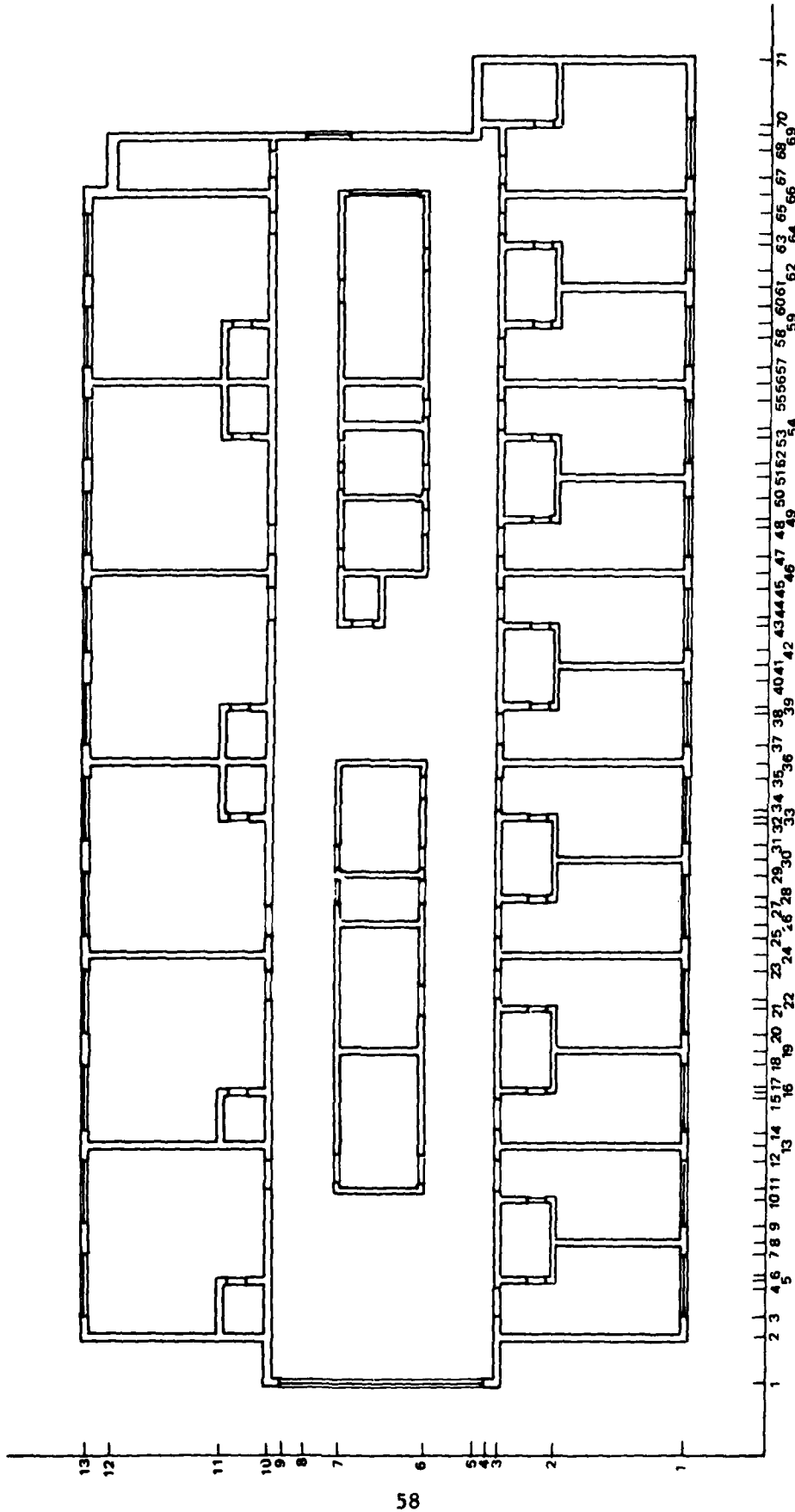
HENRY R. LANDIS STATE HOSPITAL

Figure 24 Orthogonal Grid for Landis Hospital.

58

Table IV   Grid Dimensions, Henry R. Landis State Hospital.

	DIMX				DIMY
1 —	1.829	36 —	.609	1 —	5.080
2 —	.762	37 —	1.117	2 —	2.133
3 —	1.117	38 —	.254	3 —	.203
4 —	.254	39 —	1.067	4 —	.203
5 —	.508	40 —	.609	5 —	2.146
6 —	.559	41 —	.609	6 —	3.580
7 —	.609	42 —	1.067	7 —	.997
8 —	.609	43 —	.254	8 —	1.352
9 —	1.067	44 —	1.117	9 —	.203
10 —	.254	45 —	.609	10 —	1.829
11 —	1.117	46 —	.609	11 —	4.140
12 —	.609	47 —	1.117	12 —	1.041
13 —	.609	48 —	.254		
14 —	1.117	49 —	1.067		
15 —	.254	50 —	.609		
16 —	.508	51 —	.609		
17 —	.559	52 —	1.067		
18 —	.609	53 —	.254		
19 —	.609	54 —	1.117		
20 —	1.067	55 —	.609		
21 —	.254	56 —	.609		
22 —	1.117	57 —	1.117		
23 —	.609	58 —	.254		
24 —	.609	59 —	1.067		
25 —	.565	60 —	.609		
26 —	.552	61 —	.609		
27 —	.254	62 —	1.067		
28 —	1.067	63 —	.254		
29 —	.609	64 —	1.117		
30 —	.609	65 —	.609		
31 —	.559	66 —	.609		
32 —	.508	67 —	1.117		
33 —	.254	68 —	.406		
34 —	1.117	69 —	.914		
35 —	.609	70 —	2.235		

ALL DIMENSIONS IN METERS

Blast
Front

TIME= 0.005 SECS
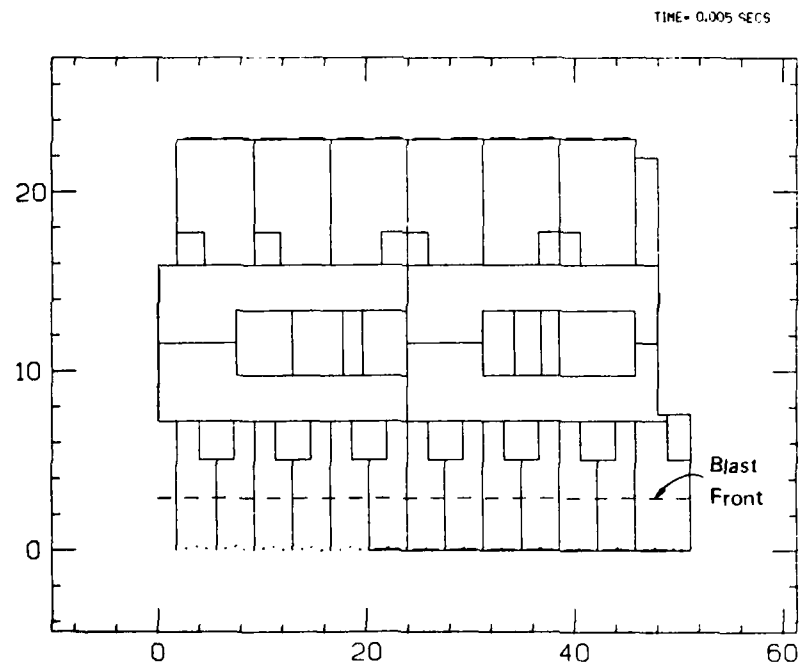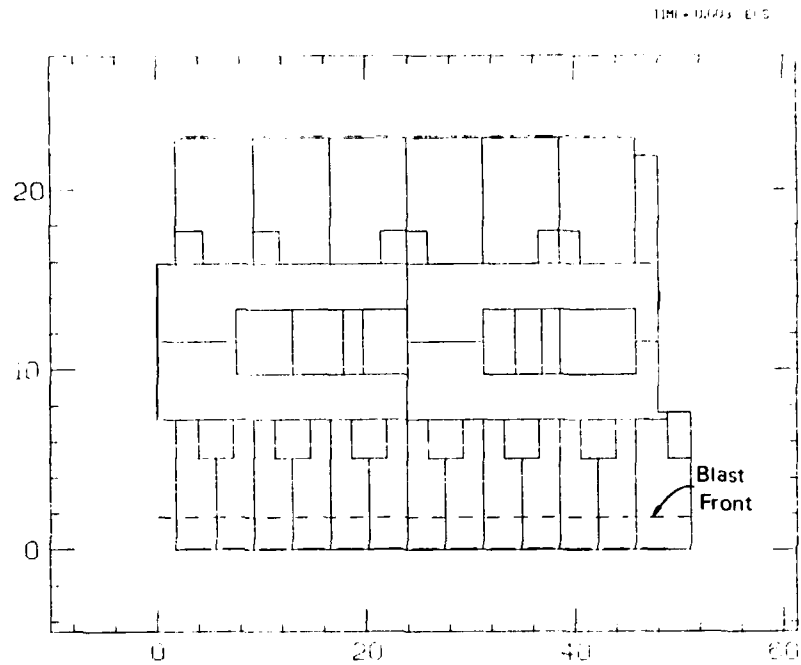
Blast
Front

Figure 25   BRACOB Simulation of Blast Response of Landis Hospital.

60

VI CONCLUSIONS AND RECOMMENDATIONS

The wall collapse (BRACOB) and debris transport (DEBRIS) simulations
appear now to begin serving as aids in understanding the fire-blast
interaction. Wall failure sequences and debris locations and timing
are reasonably well simulated, provided transport is over relatively
short distances. However, long-distance transport, even of heavy
masonry fragments, does not appear satisfactory and requires investiga-
tion of the fragment departure velocities and a possible ground-
fragment interaction.

In addition to seeking corrections for these deficiencies, it is
recommended that a field test opportunity be sought to test the
theories of debris creation and short-range transport from wall
masonry buildings.

REFERENCES

1. Wiehle, C. K., and J. L. Bockholt, "Existing Structures Evaluation,
    Part I: Walls," for Office of Civil Defense, Stanford Research
    Institute, Menlo Park, California (November 1968)   AD-687 293 .

2. Wiehle, C. K., and J. L. Bockholt, "Existing Structures Evaluation
    Part IV: Two-way Action Walls," for Office of Civil Defense,
    Stanford Research Institute, Menlo Park, California (September 1970)
    AD-719 306.

3. Hoerner, S., Fluid Dynamic Drag, published by author, 1958.

4. Hoerner, S., and H. Borst, Fluid Dynamic Lift, published by Mrs.
    Liselotte A. Hoerner, 1975.

5. Fletcher, E., R. W. Albright, V. Goldizen, and I. Bowen, "Determi-
    nations of Aerodynamic-Drag Parameters of Small Irregular Objects
    by Means of Drop Tests," Lovelace Foundation for Medical Education
    and Research (June 1960).

6. Warren, R. E., "Debris Studies Compendium," Bell Laboratories for
    U. S. Army Ballistic Missile Defense Systems Command (15 September
    1974).

7. Longinow, A., private communication.

8. Goldstein, H., Classical Mechanics (Addison-Wesley, 1959).

9. Warren, R., "Tree and Automobile Debris/DIAL PACK Event," Bell
    Telephone Laboratories for Defense Nuclear Agency (August 1973).

10. Fletcher, E. R. and I. G. Bowen, "Blast-Induced Translational
    Effects," Annals of the New York Academy of Sciences, Vol. 152,
    Art. 1, pp. 378 - 402 (Oct. 29, 1968).

11. Randall, P. A., "Damage to Conventional and Special Types of Residences
    Exposed to Nuclear Effects" Operation TEAPOT, WT-1194 (April 12, 1961),
    AD 611160.

12. Witt, E., "Blast Transport of Debris from Scale Model Buildings,"
    Bell Telephone Laboratories, Inc., for Defense Nuclear Agency
    (January 1979).

13. Dudash, M., ed., "Operation Prairie Flat Symposium Report,"
    General Electric TEMPO for Defense Atomic Support Agency,
    (January 1979).

14. Rempel, J. and C. K. Wiehle, "Collateral Air Blast Damage"
    SRI International for Defense Nuclear Agency (April 1978).

15. Taylor, B., "Blast Effects of Atomic Weapons upon Curtain Walls
    and Partitions of Masonry and other Materials/Operation Upshot
    Knothole Project 3.29," Federal Civil Defense Administration
    (August 1956).

16. Wiehle, C. K., J. R. Rempel and J. F. Beck, "MIDDLE NORTH SERIES
    DICE THROW EVENT, Dynamic Response of Two Types of German
    House Construction", SRI International for Defense Nuclear Agency
    (October 1978), POR 6966.

MANDATORY STANDARD DISTRIBUTION LIST FOR RESEARCH REPORTS
(ALL PROJECTS)

(Number of Copies - One unless otherwise indicated)

Federal Emergency Management Agency
Mitigation and Research
ATTN: Administrative Officer
Washington, D.C. 20472   (60)

Assistant Secretary of the Army (R&D)
ATTN: Assistant for Research
Washington, D.C. 20301

Chief of Naval Research
Washington, D.C. 20306

Defense Technical Information Center
Cameron Station
Alexandria, Virginia 22314   (12)

Oak Ridge National Laboratory
ATTN: Librarian
P.O. Box X
Oak Ridge, Tennessee 37830

Mr. Phillip M. Smith
Associate Director,
Natural Resouces & Commercial Services
Office of Science and Technology Policy
Executive Office Bldg.
Washington, D.C. 20500

Los Alamos Scientific Laboratory
ATTN: Document Library
Los Alamos, N.M. 87544

The RAND Corporation
ATTN: Document Library
1700 Main Street
Santa Monica, CA 90401

Naval Ship and Development Center
Attn: Mr. Tom Amrhein
Code 857
Washington, D.C. 20034

Command and Control Technical Center
Department of Defense
Room 2E312 Pentagon
Washington, D.C. 20301

Mr. A.P. Brackebusch
Forest Fire Research
Northern Forest Fire Laboratory
Missoula, Montana 59801

U.S. Forest Service
Attn: Dr. A Broido
P.O.Box 245
Berkeley, CA 94710

Dr. Ing P.G. Seeger
Forschungsstelle fur Brandschutztechnik
Univerisyt of Karlsruhe (TH)
75 Karlsruhe 21
Postfach 63380
West Germany

Mr. Anatole Longinow
IIT Research Institute
10 West 35th Street
Chicago, Illinois 60616

Dr. Clarence R. Mehl
Division 1112
Sandia National Laboratories
Box 5800
Albuquerque, New Mexico 87185

Hudson Institute
Quaker Ridge Road
Croton-on-Hudson
New York, 10520

Fire Research Section
Department of Structural Research
Southwest Research Institute
8500 Culebra Road
San Antonia, Texas 78206

Factory Mutual Research Corp.
Attn: Dr. Raymond Friedman
1151 Boston-Providence Turnpike
Norwood, Massachusetts 02062

Mr. Edward L. Hill
Research Triangle Institute
Post Office Box 12194
Research Triangle Park, N.C. 27709

Mr. Arthur D. Caster
Chairman, Coordination Committee
  on Civil Defense
American Society of Civil Engineers
2864 McFarlan Park Drive
Cincinnati, Ohio 45211

Mr. Norman J. Alvares
Lawrence Livermore Laboratory
Box 808, L-Stop 442
Livermore, CA 94550

Dr. Conrad V. Chester
Oak Ridge National Laboratory
P.O.Box X
Oak Ridge, Tennessee 37830

Mr. Marvin Drake
Scientific Applications, Inc.
P.O.Box 2351
1200 prospect Street
La Jolla, CA 92037

Professor A. Murty Kanury
Department of Aerospace and
  Mechanical Engineering
University of Notre Dame
Notre Dame, Indiana 46556

Dr. Stanford S. Penner
6424 Lavton Avenue
Oakland, CA 94618

Mr. Thomas C. Goodale
SRI International
Menlo Park, CA 94025

Mr. H.L. Murphy
P.O.Box 1727
San Mateo, CA 94401

Mrs. Ruth W. Schnider
Center for Planning and Research, Inc.
2483 East Bayshore Road
Palo Alto, CA 94303

Mr. Walmer (Jerry) Strope
5600 Columbia Pike (Suite 101)
Bailey's Crossroads, VA 22041

Mr. Don Sachs
Kaman Nuclear
Garden of the Gods Road
Colorado Springs, Colorado 80901

Prof. R.K. Pefley
University of Santa Clara
Santa Clara, CA 95053

Chief Robert G. Purington
Lawrence Livermore Laboratory
University of California
P.O.Box 808, L-519
Livermore, CA 94550

Mr. William Taylor
Ballistic Research Laboratories
Aberdeen Proving Grounds, MD 21005

Mr. Ronald Drzewoeclo
Calspon Corporation
P.O.Box 235
Buffalo, New York 15221

National Fire Protection Association
    Library
470 Atlantic Avenue
Boston, Massachusetts 02210

Science Information Exchange
Attn: Dr. Vincent Maturi
Suite 209
1730 M Street, N.W.
Washington, D.C. 20036

Mr. J. Thomas Hughes
U.S. Fire Administration
Washington, D.C. 20230

Dr. Don Scheuch
SRI International
Menlo Park, CA 94025

Dr. Geoffrey N. Berlin
National Fire Protection Association
470 Atlantic Avenue
Boston, Massachusetts 02210

Dr. Forman A. Williams
Department of the Aerospace
    and Engineering Sciences
University of California San Diego
La Jolla, CA 03027

Mr. Leo A. Schmidt
Institute for Defense Analuses
Program Analusis Division
400 Army-Navy Drive
Arlington, VA 22202

 Chief Joint Civil Defense
    Support Group
Office, Chief of Engineers
Department of the Army
Attn: ENGMC-D
Washington, D.C. 20314

Director, U.S. Army Ballistic
    Research Laboratory
Attn: Document Library
Aberdeen Proving Ground, MD 21005

Director, U.S. Army Engineer
    Waterways Experiment Station
P.O. Box 611
Attn: Document Library
Vicksburgh, Mississippi 39180

Air Force Weapons, Lab.
Attn: SUL Technical Library
Kirtland Air Force Base
Albuquerque, New Mexico 87117

Civil Engineering Center/AF/PRECET
Wright Patterson Air Force Base
Ohio, 45433

Dr. William F. Christian
Underwriters laboratories, Inc.
333 Pfingsten Road
Northbrook, Illinois 60062

Mr. W.L. Huff
USAE Waterways Experiment Station
Post Office Box 631
Vicksburg, Mississippi 39180

Mr. Richard Laurino
Center for Planning and Research
2483 East Bayshore - Suite 104
Palo Alto, California 94303

Mr. Joseph E. Minor
Texas Technological College
Lubbock, Texas 79408

Mr. Ashton M. Patterson
Canadian Defense Research Staff
2450 Massachusetts Ave., N.W.
Washington, D.C. 20008

Mr. Carl Wiehle
Defense Intelligence Agency
Attn: CKW DB-4C2
Washington, D.C. 20301

Dr. Steve J. Wiersma
International Power Technology
506 Oakmead Parkway
Sunnyvale, CA 94025

Mr. C. Wilton
Scientific Services, Inc.
517 East Bayshore Drive
Redwood City, CA 94060

Mr. Fred Sauer
Physics International Company
2700 Merced Street
San Leandro, CA 94577

The Dikewood Corporation
1008 Bradbury Drive, S.E.
University Research Park
Albuquerque, New Mexico 87106

Mr. Irwin A. Benjamin
Building Research Division
National Bureau of Standards
Washington, D.C. 20234

Fire Research Library
National Bureau of Standards
Technology Building 225
Washington, D.C. 20234

U.S. Naval Civil Engineering Library
Attn: Document Library
Port Hueneme, CA 93041

Chief of Engineers
Department of the Army
Attn: ENGEME-RD
Washington, D.C. 20314

Mr. Howard McClennon, President
International Association of Fire
    Fighters
815 16th Street, N.W.
Washington, D.C. 20006

The Information Center
Forest Fire Research Institute
331 Cooper Street
Ottawa Ontario
CANADA KIA 043

U.S. Army Training and Doctrine
    Command
Fort Monroe
Hampton, VA 23651

U.S. Army Combined Arms Combat
    Development Activity
Fort Leavensworth, KA 66027

Mr. Clay P. Butler
1427 Floribunda
Burlingame, CA 94010

Dr. Francis E. Fendell
R1/1038
TRW
One Space Park
Redondo Beach, CA 90178

Raymond Alger
SRI International
Menlo Park, CA 94025

Geoffrey N. Berlin
National Fire Protection Association
470 Atlantic Avenue
Boston, Massachusetts 02210

Jana Backovsky
Perkins Hall 417
Harvard University
Cambridge, Massachusetts 02138

Tom Blake
Systems Science & Software
P.O.Box 1620
La Jolla, CA 92138

Craig Chandler, Director
Forest Fire & Atmospheric Science Res.
U.S. Forest Service
Department of Agriculture
Washington, D.C. 20250

John E. Cockayne
Senior Scientist
Science Applications, Inc.
1710 Goodridge Drive
P.O.Box 1303
McLain, VA 22101

Dick Foster
SRI International
1611 Kent Street
Arlington, VA 22209

Robert Fristrom
Applied Physics Lab/JHU
Johns Hopkins Road
Laurel, MD 20810

National Council & Radiation
  Protection & Measurements
7910 Woodmont Avenue
Bethesda, MD   20014

Mr. John Rempel
   International
        94025

Mr. Thomas Waterman
IITRI
10 W. 35th Street
Chicago, Illinois 60616

Emergency Technology Division
Oak Ridge National Laboratory
P.O.Box
Oak Ridge, Tennessee 37830
Attn: Librarian

Director
Lovelace Foundation
5200 Gibson Boulevard, S.E.
Albuquerque, New Mexico 87108

Dr. Rudolf J. Engelmann
Department of Energy
Dept of Military Application
Washington, D.C. 20545

Technology & Management Consultants
330 Washington Street
Suite 613
Marina Del Rey, CA 90291

R&D Associates
Attn: Dr. Henry Cooper
1401 Wilson Blvd., Rosslyn, VA 22209

Director, Army Materials and
    Mechanics Research Center
Attn: Technical Library
Watertown, Massachusetts 02172

Dr. Lewis V. Spencer
National Bureau of Standards
Room C313-Building 245
Washington, D.C. 20234

Mr. Samuel Kramer, Chief
Office of Federal Building
  Technology
Center ofr Building Technology
National Bureau of Standards
Washington, D.C. 20234

Mr. William Parker
National Bureau of Standards
Room B66, Technology Bldg.
Washington, D.C. 20234

AFWL/Civil Engineering Division
Kirtland Air Force Base
New Mexico 87117

Los Alamos Scientific Lab.
Attn: Document Library
Los Alamos, New Mexico 87544

Pacific -Sierra Research Corp.
Attn: Harold L. Brode
1456 Cloverfield Blvd.
Santa Monica, CA 90904

Higgins, Auld & Associates Engineers
Attn: Cornelius J. Higgins
2601 Wyoming Blvd., Suite H-1
Albuquerque, New Mexico 87112

Center for Planning and Research, Inc.
2483 East Bayshore - Suite 104
Palo Alto, CA 94304

Mr. Kenneth Kaplan
Management Science Associates
P.O.Box 239
Los Altos, CA 94022

Stanley Martin
SRI International
Menlo Park, CA 94025

Laurence Pietrzak
Mission Research Corp.
735 State Street, P.O. Drawer 719
Santa Barbara, CA 93102

Fred Offensend
SRI International
Menlo Park, CA 94025

John Rockett
National Bureau of Standards
Center for Fire Research
Building 225, Room A17
Washington, D.C. 20234

Wilhelm Sjolin
Research Institute of National Defense
Forsvarets Forskningsanstalt
Stockholm 80, Sweden

Richard Small
R&D Associates
P.O.Box 9695
Marina del Rey, CA 90291

REPORT DOCUMENTATION PAGE		READ INSTRUCTIONS BEFORE COMPLETING FORM
1. REPORT NUMBER	2. GOVT ACCESSION NO. AD-AC89/7C	3. RECIPIENT'S CATALOG NUMBER
4. TITLE (and Subtitle) DEBRIS DISTRIBUTION AS A PARAMETER IN BLAST/FIRE INTERACTION		5. TYPE OF REPORT & PERIOD COVERED Final Report May, 1979 to July, 1980
		6. PERFORMING ORG. REPORT NUMBER HSU-8561
7. AUTHOR(s) John R. Rempel		8. CONTRACT OR GRANT NUMBER(s) DCPA01-79-C-0269
9. PERFORMING ORGANIZATION NAME AND ADDRESS SRI International Menlo Park CA 94025		10. PROGRAM ELEMENT, PROJECT, TASK AREA & WORK UNIT NUMBERS DCPA Work Unit 2564C
11. CONTROLLING OFFICE NAME AND ADDRESS Federal Emergency Management Agency Washington, D.C. 20472		12. REPORT DATE June 1980 13. NO. OF PAGES 63
14. MONITORING AGENCY NAME & ADDRESS (if diff. from Controlling Office)		15. SECURITY CLASS. (of this report) Unclassified
		15a. DECLASSIFICATION/DOWNGRADING SCHEDULE

16. DISTRIBUTION STATEMENT (of this report)

Approved for public release; distribution unlimited.

17. DISTRIBUTION STATEMENT (of the abstract entered in Block 20, if different from report)

18. SUPPLEMENTARY NOTES

19. KEY WORDS (Continue on reverse side if necessary and identify by block number)

debris, air blast, building collapse, fire/blast interaction

20. ABSTRACT (Continue on reverse side if necessary and identify by block number)

By applying the principles of classical mechanics and approximating aerodynamic
and ground interaction forces, a general three dimensional debris fragment
transport code DEBRIS has been written. Certain field experiments using
airblast originating in large H.E. explosions have been simulated and the simul-
ated and experimental outcomes compared. While simulation of long distance or
high speed transport by tumbling or sliding over ground surfaces is not satis-
factory, short distance transport such as might be found following structural

DD FORM 1473 1 JAN 73

EDITION OF 1 NOV 65 IS OBSOLETE

19. KEY WORDS (Continued)

20 ABSTRACT (Continued)

collapse is sufficiently realistic that DEBRIS combined with a previously
developed building response code BRACOB appears ultimately capable of describing
outside wall debris patterns.   It is recommended that velocity dependent loss
mechanisms be incorporated in DEBRIS to improve its simulation of long distance
transport and that certain existing uncertainties concerning wall debris
creation and transport be lessened by means of a full size or near full size
field experiment.

LME